

ADVANCED OPTICAL MATERIALS

Supporting Information

for *Adv. Optical Mater.*, DOI 10.1002/adom.202302833

Golden Plasmophores with Tunable Photoluminescence and Outstanding Thermal and Photothermal Stability

Mustafa Gharib, A. J. Yates, Stephen Sanders, Johannes Gebauer, Sebastian Graf, Anna Rosa Ziefuß, Nonappa, Günther Kassier, Christoph Rehbock, Stephan Barcikowski, Horst Weller, Alessandro Alabastri, Peter Nordlander, Wolfgang J. Parak* and Indranath Chakraborty**

Golden Plasmaphores with Tunable Photoluminescence and Outstanding Thermal and Photothermal Stability

Mustafa Gharib^{1,2}, A J Yates³, Stephen Sanders⁴, Johannes Gebauer¹, Sebastian Graf⁵, Anna Rosa Ziefuß⁶, Nonappa⁷, Günther Kassier⁸, Christoph Rehbock⁶, Stephan Barcikowski⁶, Horst Weller⁵, Alessandro Alabastri⁴, Peter Nordlander^{3}, Wolfgang J Parak^{1*} and Indranath Chakraborty^{1,9*}*

¹Center for Hybrid Nanostructure (CHyN), University of Hamburg, 22761, Hamburg, Germany

²Radiation Biology Department, Egyptian Atomic Energy Authority (EAEA), 11787, Cairo, Egypt

³Department of Physics and Astronomy, Rice University, Texas, Houston, USA

⁴Department of Electrical and Computer Engineering, Rice University, Texas, Houston, USA

⁵Department of Chemistry, Universität Hamburg, 20146, Hamburg, Germany

⁶Department of Technical Chemistry I, University of Duisburg-Essen and Center for Nanointegration Duisburg-Essen (CENIDE), 45141, Essen, Germany

⁷Faculty of Engineering and Natural Sciences, Tampere University, Tampere, FI 33720 Finland

⁸Max Planck Institute for the Structure and Dynamics of Matter, Geb. 99 (CFEL), Luruper Chaussee 149, 22761Hamburg, Germany

⁹School of Nano Science and Technology, Indian Institute of Technology Kharagpur, Kharagpur 721302, India

*Corresponding authors: indranath@iitkgp.ac.in (IC), wolfgang.parak@uni-hamburg.de (WJP), nordland@rice.edu (PN).

Supporting Information

Index

1. Synthesis of CTAB-coated gold nanorods (GNRs@CTAB)
2. Synthesis of GSH-capped gold nanoclusters (GNCs@GSH)
3. Synthesis of polyelectrolyte-coated gold nanorods (GNRs@LBL)
4. Synthesis of silica-coated gold nanorods (GNRs@SiO₂)
5. Synthesis of GNCs-coated gold nanorods (GNRs@GNCs)
6. Synthesis of GNCs-coated polyelectrolyte-functionalized gold nanorods (GNRs@LBL@GNCs)
7. Synthesis of GNCs-coated silica-functionalized gold nanorods (GNRs@SiO₂@GNCs plasmophores)
8. Synthesis of other NC-functionalized silica-coated GNRs
9. Colloidal stability of GNRs@CTAB, GNRs@GNCs, GNRs@LBL@GNCs, and GNRs@SiO₂@GNCs plasmophores
10. Tuning silica shell thickness of the GNRs@SiO₂@GNCs plasmophores
11. Photophysical properties of the GNRs@SiO₂@GNCs plasmophores
12. Thermal stability of GNRs@CTAB, GNRs@SiO₂, and GNRs@SiO₂@GNCs plasmophores
13. Photothermal stability of GNRs@CTAB, GNRs@SiO₂, and GNRs@SiO₂@GNCs plasmophores
14. Photoluminescence stability in O₂- and Ar-enriched environments
15. Photostability of GNRs@SiO₂@GNCs plasmophores vs. GNCs
16. Lumerical calculations of optical properties of GNRs@SiO₂@GNCs plasmophores
17. Photothermal simulations of GNRs@SiO₂@GNCs plasmophores
18. References

Materials

Before use, all glassware was washed with aqua regia (3:1 (v/v) conc. HCl/conc. HNO₃) followed by rinsing with copious amounts of Milli-Q water. Chloroauric acid (HAuCl₄) was purchased from Alfa Aesar, sodium citrate, L-glutathione (GSH), silver nitrate (AgNO₃), ascorbic acid (AA), sodium borohydride (NaBH₄), hexadecyltrimethylammonium bromide (CTAB), hydrochloric acid (HCl), methanol (MeOH), tetraethyl orthosilicate (TEOS), N-hydroxysuccinimide (NSH), 1-ethyl-3-(3-dimethylaminopropyl)carbodiimide (EDC), polyvinylpyrrolidone (PVP), poly(diallyldimethylammonium chloride) (PDADMAC), poly(styrenesulfonate) (PSS), bovine serum albumin (BSA), and (±)-α-lipoic acid (LA, ≥ 99%) were purchased from Sigma-Aldrich, 3-aminopropyl triethoxysilane (APTES) was purchased from Fluka. 4-(2 hydroxyethyl)-1-piperazineethanesulfonic acid (HEPES) was purchased from

Biochrom. Sodium oleate (NaOL) was purchased from TCI, sodium chloride (NaCl, 99.9%) and sodium hydroxide (NaOH) were purchased from Roth. Phosphate-buffered saline (PBS), Dulbecco's Modified Eagle Medium (DMEM), Roswell Park Memorial Institute culture medium (RPMI), and fetal bovine serum (FBS) were purchased from ThermoFischer.

Characterization of NPs

The successful synthesis and functionalization of different NPs was confirmed using UV-vis absorption and fluorescence spectroscopy. The UV-vis absorption spectra were obtained using an Agilent 8453 UV-vis spectrophotometer, whereas, fluorescence spectra were recorded with a Fluorolog fluorescence spectrophotometer equipped with a 450 W Xe-lamp (FL3-22, Horiba Jobin Yvon Inc.), using 1 cm path length quartz cuvettes. The hydrodynamic diameters (d_h) and zeta potentials (ζ) of the NPs were analyzed using dynamic light scattering (DLS) and particle electrophoresis techniques with a Malvern Zetasizer Nanoparticle analyzer (ZEN 3600).

The size and morphology of the obtained NPs was investigated using a JEOL JEM-2100F-UHR field emission gun transmission electron microscope (TEM) (JEOL, Japan), equipped with high angle annular dark field (HAADF). HRTEM images were generated using a TVIPS F216 CMOS camera (2k x 2k). Scanning transmission electron microscopy (STEM) studies were carried out in STEM mode. The TEM was operated at an accelerating voltage of 200 kV. Elemental mapping and distribution within the NPs was investigated through energy-dispersive X-ray spectroscopy (EDS) spot analysis using a Philips CM 300 UT (LaB6) TEM operating at 200 kV, supplied with SDD EDX detector (Ametek) and Gatan CCD camera. All samples were prepared prior to measurements by drop-casting on ultrathin carbon-coated copper grids (400 mesh square) and were left to dry in a Petri dish before imaging.

To visualize the three-dimensional (3D) spatial distribution and assembly of the GNCs on the silica-coated GNRs, STEM tomography reconstruction (3D-TEM) was carried out by retrieving the 3D structure of the NPs through acquiring TEM images over a tilt angle range of $\pm 74^\circ$. In brief, the samples were tilted from -74° to $+74^\circ$, with a tilt increment of 3° . The 3D reconstruction of the NPs morphology was generated by aligning the acquired TEM images concerning each other using a phase correlation procedure.[1-4]

Methods

1. Synthesis of CTAB-coated gold nanorods (GNRs@CTAB)

GNRs of different aspect ratios were synthesized using a previously reported seed-mediated route with slight modifications.[5] In brief, the seed NPs were synthesized by mixing 2.5 mL of gold precursor (HAuCl_4) solution (0.5 mM) with 2.5 mL of CTAB solution (200 mM) for 5 minutes. Then, 0.5 mL of freshly prepared NaBH_4 solution (6 mM) was injected to the reaction mixture under vigorous stirring for two minutes. The color changed immediately into brownish yellow. The seed solution was then left to age for 30-60 min at 30 °C before further use.

The growth of GNRs was carried out using a mixture of binary surfactant systems composed of CTAB and sodium oleate (NaOL). In brief, 7 g of CTAB and 1.234 g of NaOL were dissolved in 0.25 L of warm Milli-Q (MQ) water. The temperature of the solution was then brought to 30 °C. Different volumes of AgNO_3 (4 mM) were then added to grow GNRs of different AR. After 15 min, 0.25 L of 1 mM HAuCl_4 solution was mixed with the reaction mixture under moderate stirring for 1.5 h. To obtain GNRs of a desired aspect ratio (AR), the pH of the growth solution was adjusted by introducing different amounts of concentrated HCl. Next, 1.25 mL of 64 mM ascorbic acid was injected under vigorous stirring for 30 seconds. Finally, different volumes of seed solution were added under vigorous stirring for 30 seconds. The reaction mixture was left undisturbed at 30 °C overnight. The resultant GNRs were purified afterwards to get rid of excess CTAB and other impurities. To prepare the GNR solutions for further work, the CTAB concentration in the as-synthesized GNR solutions was properly adjusted. For that, 50 mL of the as-prepared GNR solution was transferred into falcon tubes and purified by two successive cycles of centrifugation at 8000 rpm for 25 min involving precipitation, discarding of the supernatant, and redissolution of the precipitate in ca. 4-5 mL of MQ water. The obtained purified solutions were collected together. The final CTAB concentration in the purified GNRs solution was ca. 15 mM. The final concentration of the purified GNRs was then calculated from their absorption values at λ_{max} of their longitudinal surface plasmon resonance (LSPR) band via the Beer-Lambert law using respective molar extinction coefficients (ϵ) values of different AR GNRs.[6]

2. Synthesis of GSH-capped gold nanoclusters (GNCs@GSH)

The GNCs@GSH were synthesized following a previously reported method with a minor modification.[7] In brief, 250 mL of the GNCs were prepared by mixing 25 mL of 20 mM aqueous solution of HAuCl_4 with 7.5 mL of 100 mM GSH solution and 217.5 mL of MQ

water under moderate stirring at 70 °C. The reaction mixture was kept at reflux for 24 h. The resultant yellow-colored and orange-fluorescent solution of GNCs@GSH was purified using centrifugal ultrafiltration (molecular weight cut-off (MWCO) = 3 kDa) and the retentate was collected and kept for further experiments.

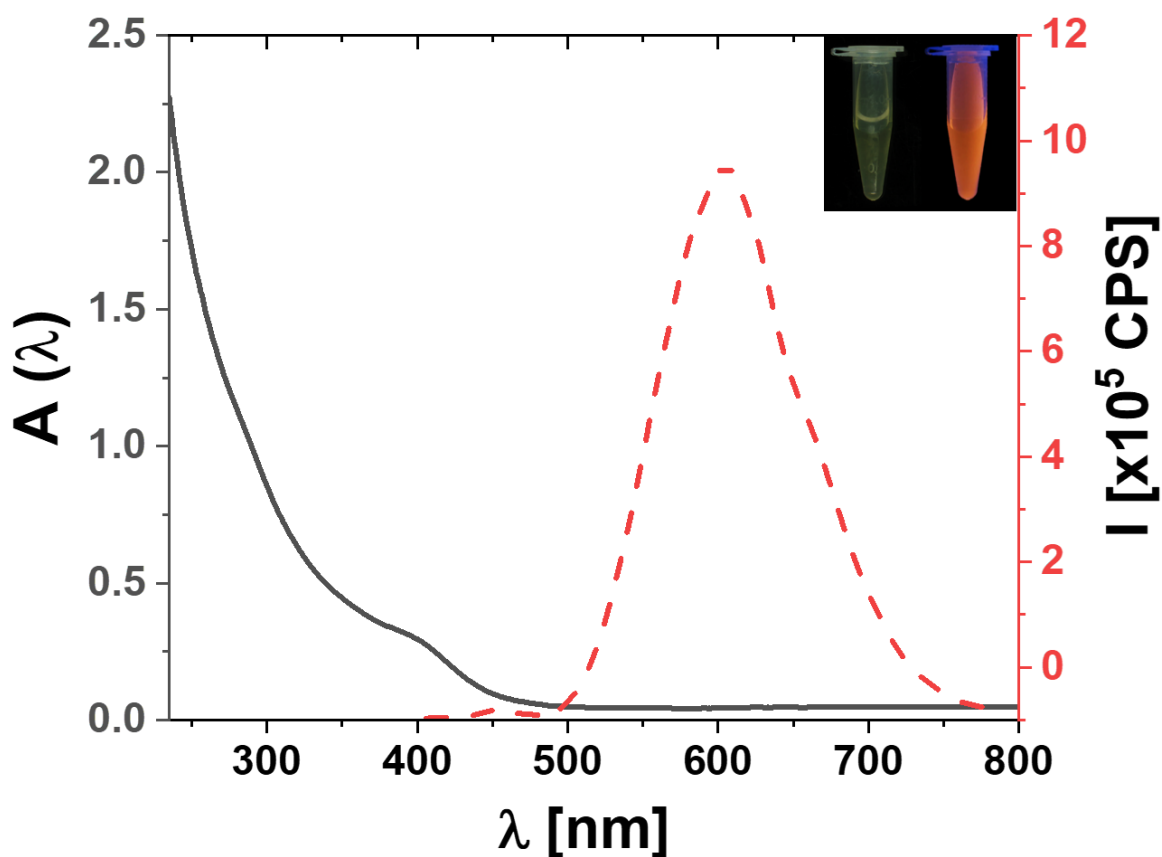


Figure S1. UV-Vis absorption (black) and fluorescence (red) spectra of GSH-GNCs. The inset is the photograph of GNCs@GSH under white light and UV light excitation.

3. Synthesis of polyelectrolyte-coated gold nanorods (GNRs@LBL)

The layer-by-layer (LBL) coating of GNRs@CTAB was performed by overcoating the GNRs with consecutive oppositely charged polyelectrolyte layers following a previous report with minor modifications.[8] In brief, 1 mL of the as-synthesized CTAB-coated GNRs was transferred into Eppendorf tubes and centrifuged at 8000 rpm for 25 min. The supernatants were removed, and the pellets were resuspended in 1 mL of 1 mM NaCl and 200 μ L of PSS solution (10 mg/mL in 1 mM NaCl). The tubes were then sonicated for 30 minutes and centrifuged afterwards at 8000 for 25 minutes to remove the unreacted PSS.

The previous steps were repeated to coat the GNRs with a second layer of polyelectrolyte by replacing the negatively charged PSS polyelectrolyte with the positively charged PDADMAC polyelectrolyte. The CTAB-coated GNRs could be overcoated by multiple layers of oppositely charged polyelectrolytes following the same method by repeating the aforementioned steps. The GNRs@LBL were then purified by two cycles of centrifugation at 8000 rpm for 25 min and the pellets were redispersed in MQ water.

4. Synthesis of silica-coated gold nanorods (GNRs@SiO₂)

The silanization of GNRs was carried out using a modification of the Stöber method[9] which is based on the hydrolysis of alkyl silicates in alcoholic solutions at alkaline pH into orthosilicic acid. The condensation of the orthosilicic acid at such reaction conditions results in the formation of silica NPs. As mentioned *vide supra*, the concentration of CTAB in the as-synthesized GNRs solution, which serves as scaffold for SiO₂ deposition, is very critical to control the thickness of the resultant silica shells around the GNRs.[10] This has been simply done by removing the free unbound CTAB from the GNR solution by successive centrifugation cycles, in a way that leaves only the minimum amount of CTAB that stabilizes the GNRs. The CTAB concentration was then adjusted by the addition of various amounts of CTAB in order to bring the final CTAB concentration in the GNRs solution below or well close to the critical micelle concentration of CTAB (0.90–0.98 mM).[10, 11] The SiO₂ deposition was initiated by the successive hydrolysis and condensation of the silica precursor, tetraethyl orthosilicate (TEOS), in alkaline reaction conditions on the CTAB micellar templates which are mostly surrounding the GNRs surfaces. Thus the SiO₂ shell thickness was determined by the ratio of silica deposited around the GNRs and freely formed silica in the solution as a function of the equilibrated CTAB added in the previous step.[10, 12, 13]

The silanization of CTAB-coated GNRs was carried out as follows, 10 mL of purified 1 nM solution of GNRs@CTAB was mixed with different volumes of 100 mM CTAB solution in 20 mL glass vials overnight to bring the final concentration of CTAB below or well close to the critical micelle concentration of CTAB (0.90-0.98 mM).[11] Then, 45 μ L of 100 mM NaOH solution was mixed with the obtained GNRs solutions for 30 min to bring the pH to 10.5 ± 0.1 . Shortly after that, 90 μ L of TEOS solution (20% in MeOH) was added dropwise over a period of 180 seconds under low stirring rate for 30 min, after which, the glass vials were removed and kept undisturbed at 30 °C for 24 h. To get rid of the free silica NPs formed apart from the plasmonic cores, the obtained solutions were purified

using five cycles of centrifugation and subsequent washing with MeOH at 9000 rpm for 30 min. The final pellets were resuspended in 5 mL of methanol using sonication and kept for further use.

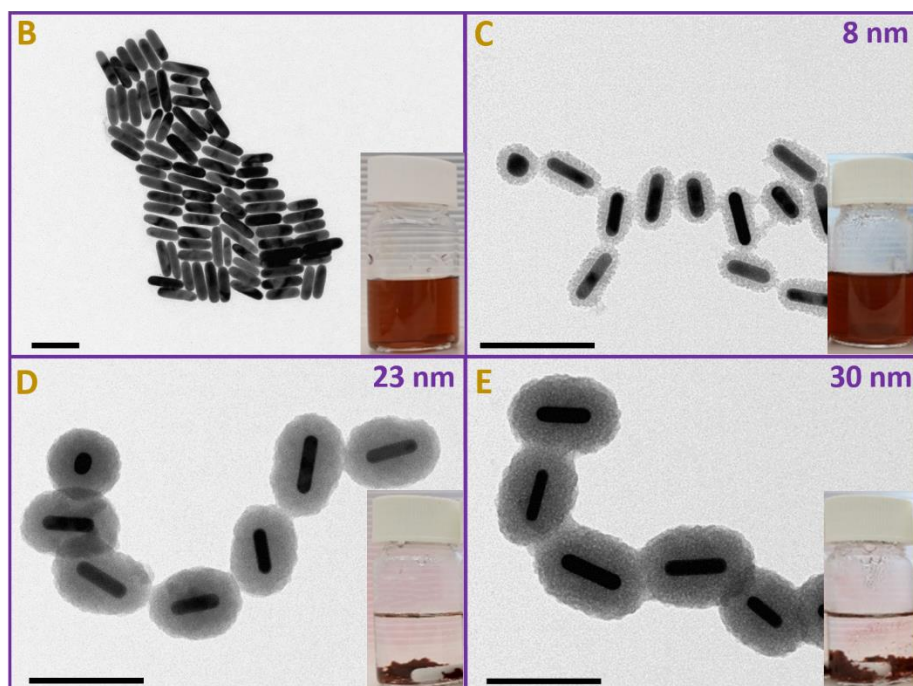
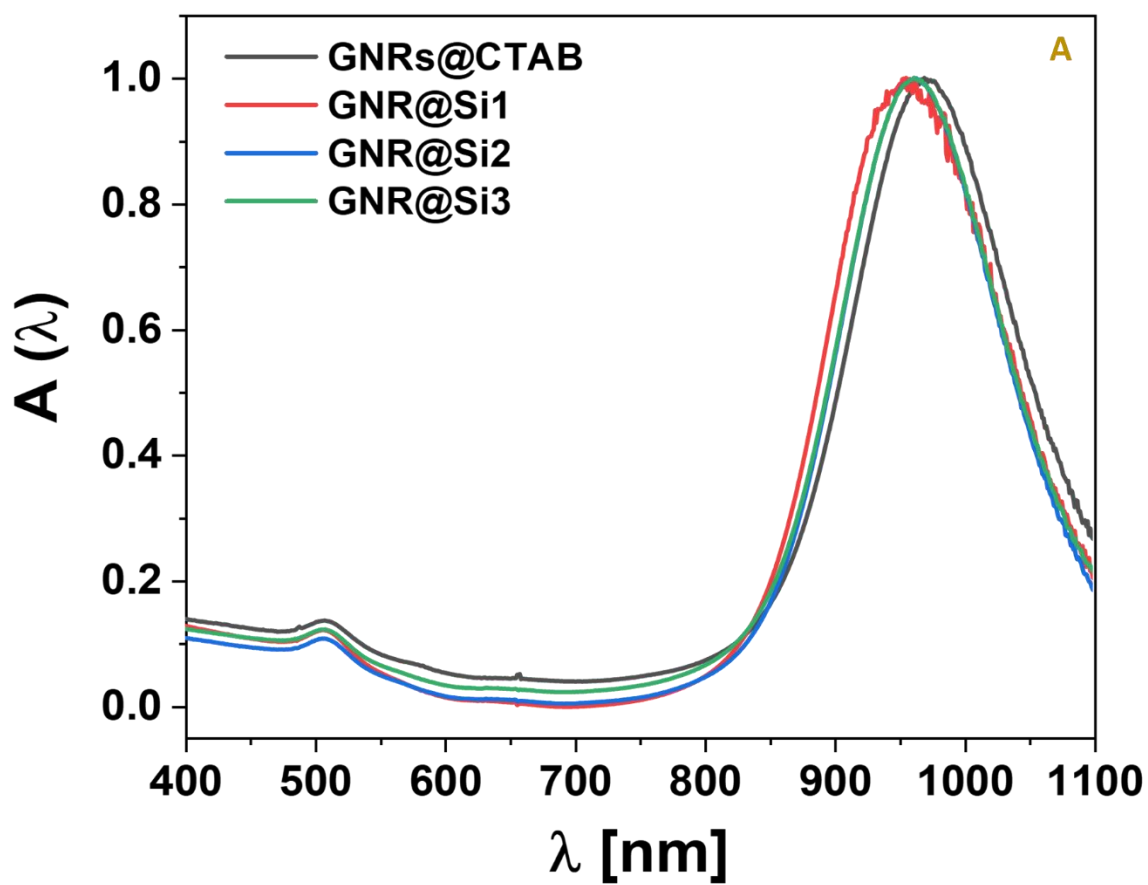


Figure S2. Tuning of the silica shell thickness of GNRs@SiO₂. (A) UV-vis absorption spectra of CTAB-coated GNRs and different silica thickness-coated GNRs (GNRs@Si1, GNRs@Si2, and GNRs@Si3), and their respective TEM images (B-E), respectively. Inset numbers indicate the corresponding silica shell thickness. Scale bar = 100 nm.

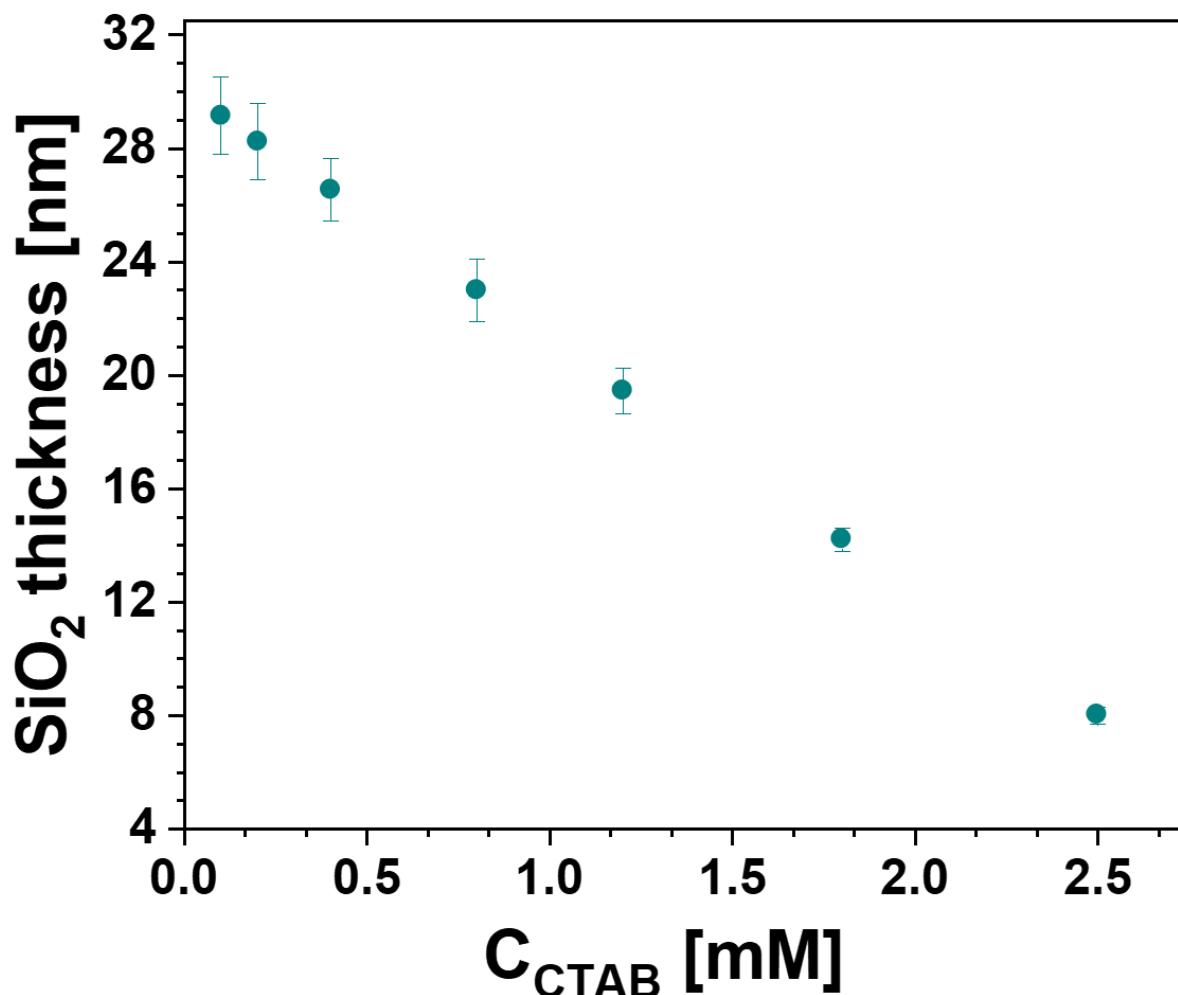


Figure S3. Free CTAB-dependent silica shell thickness of GNRs@SiO₂.

5. Synthesis of GNCs-coated gold nanorods (GNRs@GNCs)

To assess whether an electrostatic interaction between the oppositely charged GNRs and GNCs could be utilized for the synthesis of GNRs@GNCs, the following procedure was carried out: 2 mL of the positively charged CTAB-coated GNR solution was mixed with 2 mL of the negatively charged GNCs@GSH solution in a scintillation vial at 30 °C under moderate stirring for 2-3 h. The obtained solution was subsequently purified by two consecutive centrifugation cycles at 8000 rpm for 25 min and the pellet was resuspended in MQ water for further work.

6. Synthesis of GNCs-coated polyelectrolyte-functionalized gold nanorods (GNRs@LBL@GNCs)

The functionalization of GNRs@LBL with the fluorescent GNCs@GSH was carried out by mixing equal volumes of GNRs@LBL with the GNCs@GSH in a scintillation vial at 30 °C under moderate stirring for 2-3 h. The obtained solution was subsequently purified by two consecutive centrifugation cycles at 8000 rpm for 25 min and the pellet was resuspended in MQ water for further work.

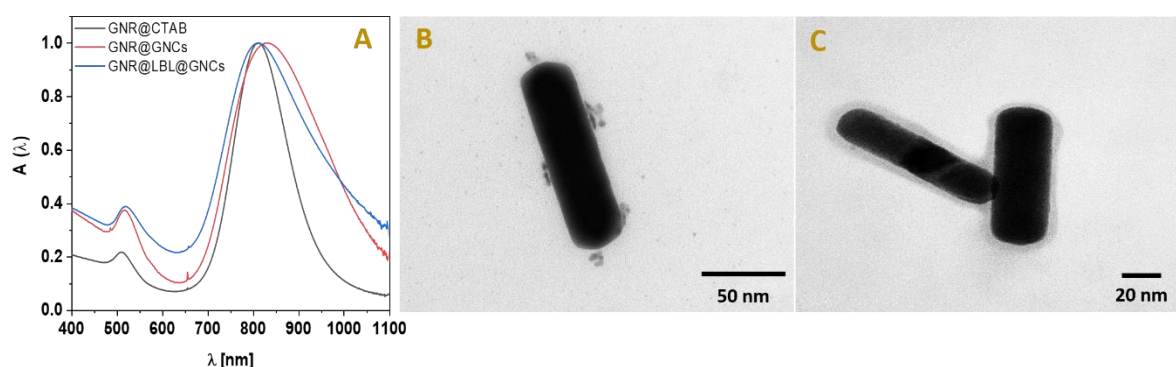


Figure S4. Characterization of GNRs@CTAB, GNRs@GNCs and GNRs@LBL@GNCs. (A) UV-vis absorption spectra of GNRs@CTAB, GNRs@GNCs, and GNRs@LBL@GNCs. TEM micrographs of GNRs@GNCs (B) and GNRs@LBL@GNCs (C).

7. Synthesis of GNCs-coated silica-functionalized gold nanorods (GNRs@SiO₂@GNCs plasmophores)

The functionalization of the silica-coated GNRs with the fluorescent GNCs@GSH was carried out using our developed method. First, the amine-modified GNRs@SiO₂ were synthesized via the interaction between GNRs@SiO₂ and APTES. In brief, 4 mL of the purified GNRs@SiO₂ was mixed with 1 mL of APTES solution (20%, MeOH) in a scintillation vial under moderate stirring at 37 °C for 24 h. The reaction mixtures were then purified by two consecutive centrifugation cycles at 5000 rpm for 45 min and the pellets were redispersed in 2 mL MQ water by sonication. The terminal carboxylic groups of GSH-capped GNCs were then activated through the carbodiimide coupling reaction. The latter reaction was carried out as follows. 1 mL of GNCs@GSH was transferred into a glass vial and mixed with 100 μ L of 100 mM EDC solution, 300 μ L of 100 mM NHS solution, and 6 mL of HEPES buffer (20 mM, pH 7.4) under vigorous stirring for 15 min at 37 °C. Shortly after that, 3 mL of the amine-functionalized GNRs (GNRs@SiO₂@APTES) were mixed with the reaction mixture and kept to react at 37 °C for 12 h under dark and moderate

stirring conditions. The resultant plasmophore solution (GNRs@SiO₂@GNCs) was purified by three consecutive centrifugation cycles at 5000 rpm for 45 min to get rid of excess GNCs. The pellets were the redispersed in MQ water and kept at room temperature for further assessments.

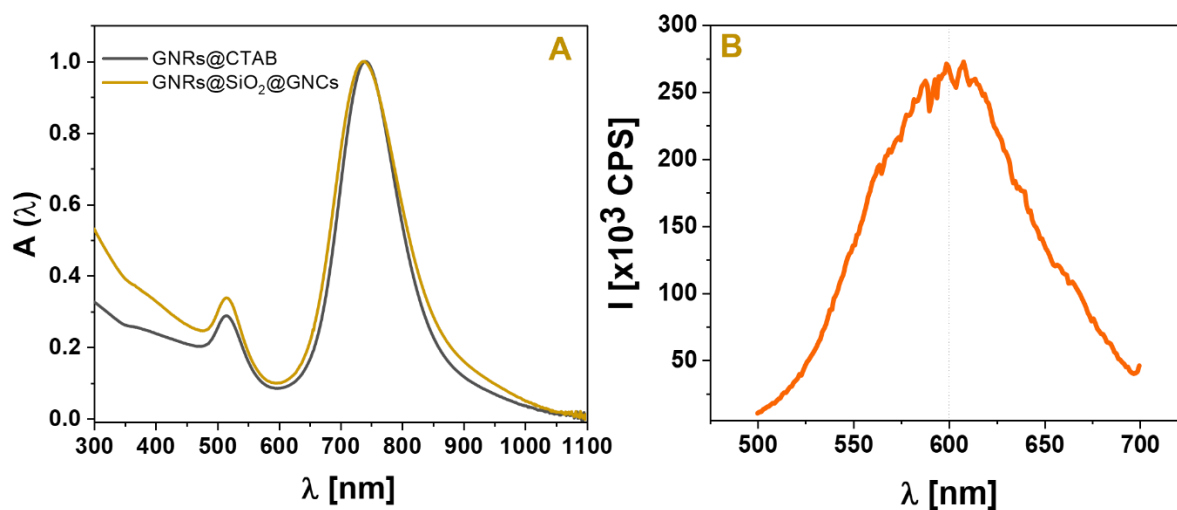


Figure S5. Characterization of GNRs@SiO₂@GNCs plasmophores. UV-vis absorption spectra (A) and photoluminescence (PL) spectra (B) of GNRs@SiO₂@GNCs plasmophores.

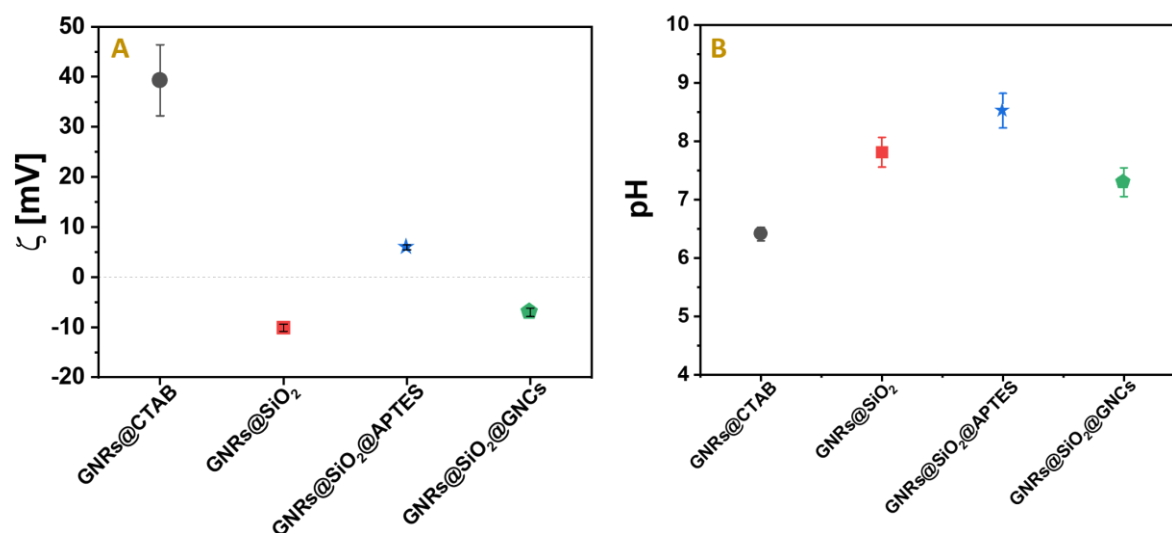


Figure S6. Zeta Potential (A) and pH (B) of GNRs@CTAB, GNRs@SiO₂, GNRs@SiO₂@APTES, and GNRs@SiO₂@GNCs.

8. Synthesis of other NC-functionalized silica-coated GNRs

In order to check the universality of our plasmophore synthesis approach, the silica-coated GNRs (GNRs@SiO₂) were conjugated with different types of NCs, namely, GNCs@BSA and dihydrolipoic acid-coated silver nanoclusters (SNCs@DHLA). First, the BSA-coated GNCs and DHLA-coated SNCs were synthesized following previously reported methods.[14, 15] Subsequently, the silica-coated GNRs were functionalized with these NCs using the same procedure followed to functionalize GNRs@SiO₂ with GNCs@GSH, just by replacing the GNCs@GSH by GNCs@BSA and SNCs@DHLA with keeping all the other conditions the same. The results showed the successful conjugation of GNRs@SiO₂ with GNCs@BSA and their distance-dependent fluorescence intensity. On the other hand, conjugation of SNCs@DHLA to the GNRs@SiO₂ resulted in the loss of their fluorescence. Nevertheless, the distance-dependent fluorescence of these plasmophores was instantly restored by adding 25 μ L of 100 mM NaBH₄ and the solutions were then centrifuged twice at 7000 rpm for 20 min and resuspended in MQ water. The results of the purified SNCs-functionalized GNRs@SiO₂ solutions exhibited a distance-dependent fluorescence intensity.

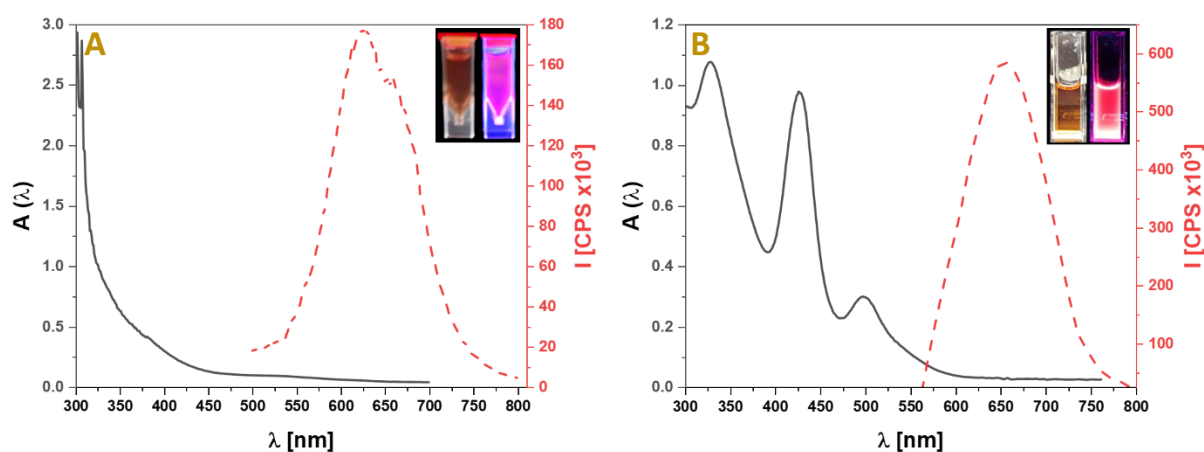


Figure S7. Characterization of GNCs@BSA and SNCs@DHLA. UV-vis absorption spectra and PL spectra of (A) GNCs@BSA and (B) SNCs@DHLA, insets are their corresponding photographs under white light (left) and UV-lamp excitation (right), respectively.

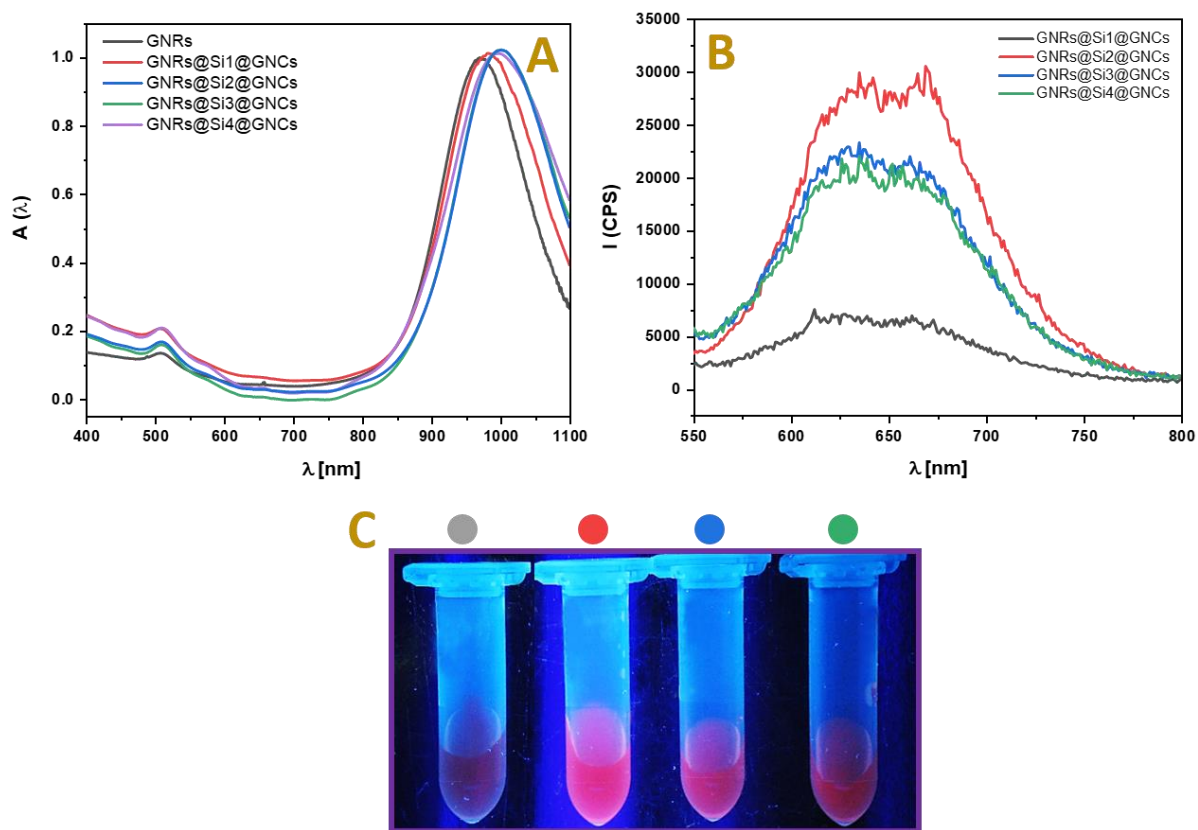


Figure S8. Functionalization of silica-coated GNRs with BSA-coated GNCs. (A) UV-vis absorption spectra of GNRs and GNRs@SiO₂@GNCs of different silica thickness (Si1-Si4). (B) PL spectra of GNRs@SiO₂@GNCs of different silica thickness and (C) their corresponding photographs under UV-lamp excitation.

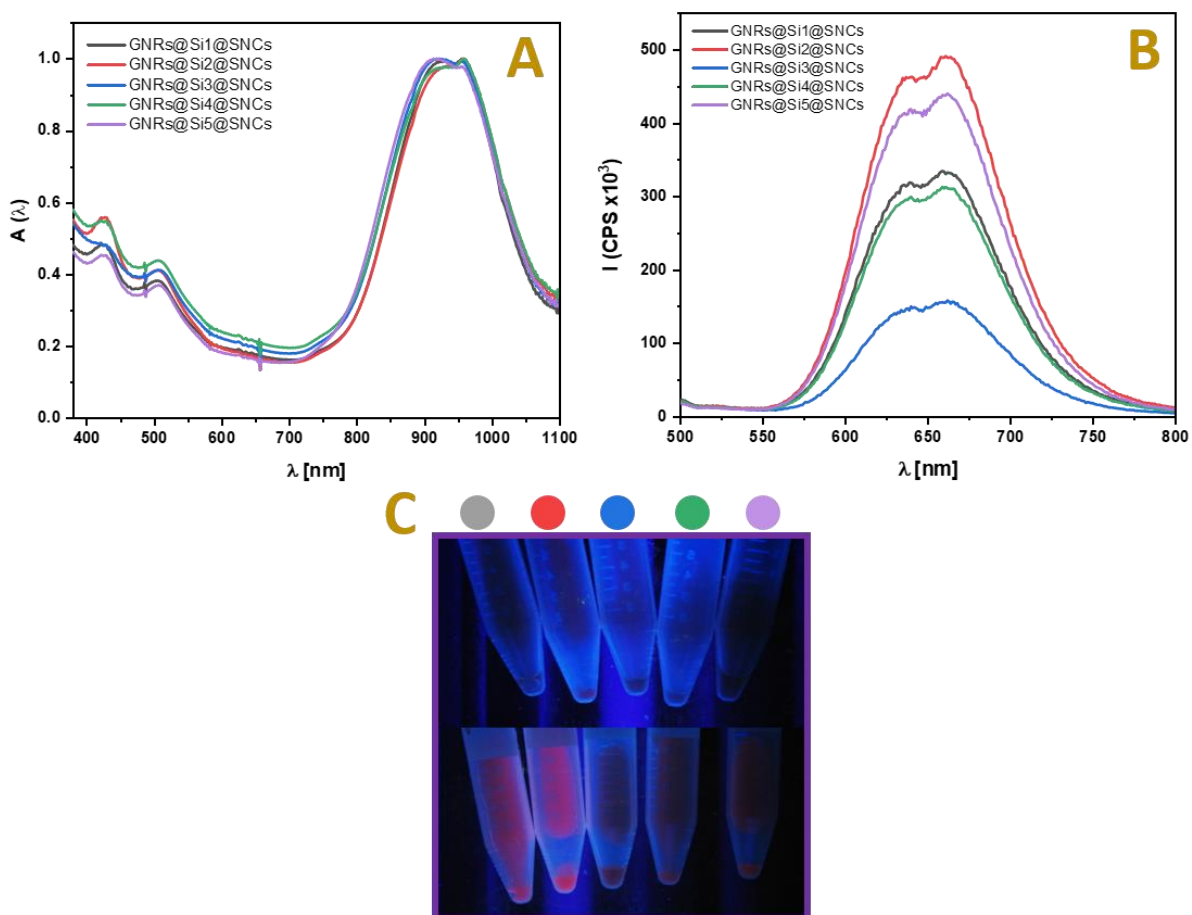


Figure S9. Functionalization of silica-coated GNRs with DHLA-coated SNCs. (A) UV-vis absorption spectra of GNRs@SiO₂@SNCs of different silica thickness (Si1-Si5). (B) PL spectra of GNRs@SiO₂@SNCs after restoration of their fluorescence and (C) their corresponding photographs under UV-lamp excitation before (upper row) and after (lower row) restoration of their fluorescence.

9. Colloidal stability of GNRs@CTAB, GNRs@GNCs, GNRs@LBL@GNCs, and GNRs@SiO₂@GNCs plasmophores

As the colloidal stability of NPs is a crucial criterion for judging the applicability of such NPs in various applications especially for biomedical applications, the colloidal stability of CTAB-capped GNRs, GNRs@GNCs, GNRs@LBL@GNCs, and GNRs@SiO₂@GNCs plasmophores was studied by recording the change in their UV-vis extinction spectra upon incubation with NaCl solutions of different ionic strength as well as with different biological media such as phosphate-buffered saline (PBS), fetal bovine serum (FBS)-free/supplemented DMEM (DMEM-FBS, DMEM+FBS, respectively), and FBS-free/supplemented RPMI (RPMI-FBS, RPMI+FBS, respectively) cell culture media at

different time points. In brief, 100 μL of NPs solutions was mixed with 900 μL of NaCl solutions of different ionic strength (25 - 1250 mM) or with 900 μL of respective biological media and the UV-vis absorption spectra of different GNRs systems were recorded at different time points (0, 6, and 24h) after incubation.

As could be revealed from (**Figure S13**), GNRs@SiO₂@GNCs plasmophores showed superb colloidal stability in NaCl solution of different ionic strength up to 24 h. Whereas, CTAB-coated GNRs started to aggregate shortly after incubation (6 h) at moderate concentration of NaCl solution (~ 600 mM) until they lost their characteristic plasmonic peaks after 24 h of incubation with 1.25 M NaCl solution (**Figure S10**). The GNRs@GNCs exhibited a very poor colloidal stability after 6 h of incubation in NaCl solution, as could be revealed from the very clear broadening of their LSPR peak. Moreover, the GNRs@GNCs completely lost their plasmonic peaks after 24 h of incubation with NaCl (**Figure S11**). In contrast, the GNRs@LBL@GNCs nanostructures were able to retain their colloidal stability and hence their spectral features at lower NaCl concentration (up to 600 mM) for up to 24 h post-incubation, however, they started to exhibit aggregation and complete loss of their plasmonic peaks at higher NaCl concentration (1.25 M) (**Figure S12**). These findings revealed that overcoating of GNRs with silica or polyelectrolyte layers render them more colloiddally stable upon incubation with NaCl solution, most probably by passivating the positively charged CTAB layer and hence their probable electrostatic interaction with the increased concentration of the negatively charged Cl⁻ ions in the medium. Such interaction results in either i) crosslinking of the GNRs leading to plasmonic coupling and broadening of LSPR plasmonic peaks or ii) surface neutralization of GNRs and hence their subsequent aggregation.

Furthermore, the UV-vis spectra of GNRs@SiO₂@GNCs plasmophores showed an excellent colloidal stability for up to 24 h post-incubation in different biological media as could be revealed from their narrow LSPR plasmonic peaks which showed no evidence for hypsochromic or bathochromic shift (**Figure S17**). The GNRs@GNCs showed also a similar trend during their incubation in different biological media (**Figure S15**). Whereas, the UV-vis spectral features exhibited by GNRs@LBL@GNCs upon incubation with different biological media revealed a moderate colloidal stability at 6 h post-incubation and the LSPR started to show considerable peak-broadening at 24 h post-incubation (**Figure S16**). It was obvious from their UV-vis absorption features that CTAB-capped GNRs showed a very poor colloidal stability in biological media as could be revealed from the

considerable peak-broadening at 6 h of incubation (**Figure S14**). These results showed again the importance of surface modification and passivating the surfaces of CTAB-capped GNRs in reducing their susceptibility to aggregation as well as to increase their robustness in relatively harsher conditions.

Based on the aforementioned findings, it is obvious that overcoating the CTAB-capped GNRs with SiO₂ shells not only allows for the effective and homogeneous deposition of GNCs on the plasmonic surfaces of GNRs in the GNRs@SiO₂@GNCs plasmaphores but also significantly enhances their colloidal stability. Moreover, it has been also reported that coating the NPs with the silica shells facilitates their functionalization with various silanes[12] and renders them more biocompatible.

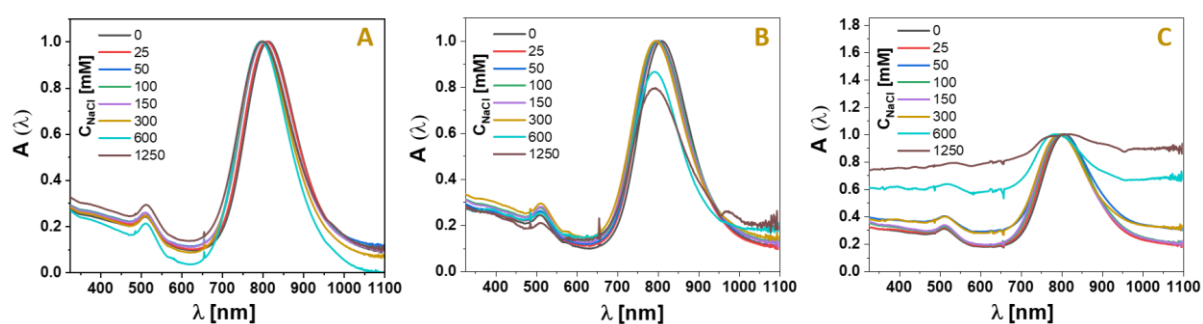


Figure S10. Colloidal stability of GNRs@CTAB in NaCl solution of different ionic strength at 0 h (A), 6 h (B), and 12 h (C).

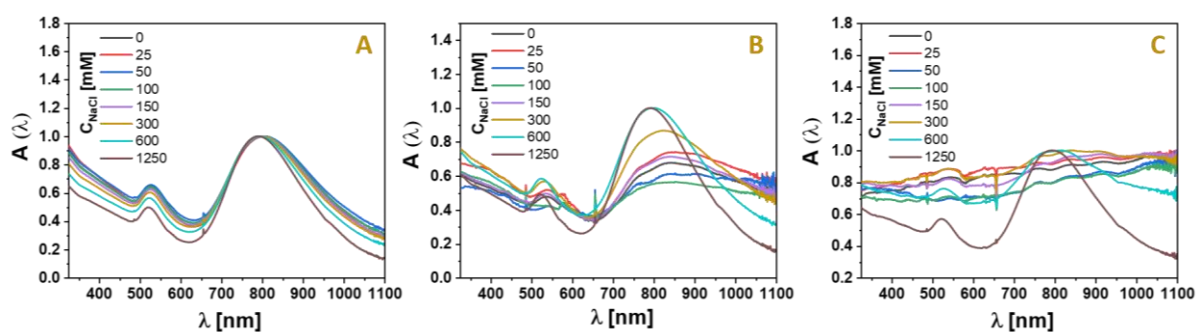


Figure S11. Colloidal stability of GNRs@GNCs in NaCl solution of different ionic strength at 0 h (A), 6 h (B), and 12 h (C).

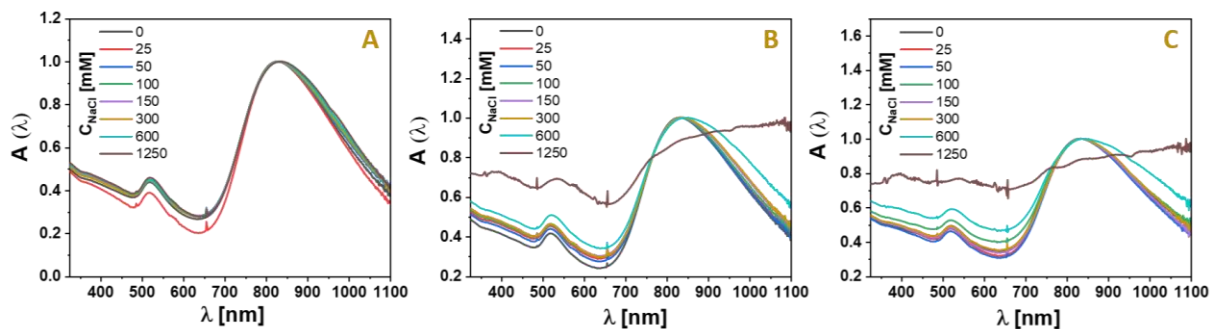


Figure S12. Colloidal stability of GNRs@LBL@GNCs in NaCl solution of different ionic strength at 0 h (A), 6 h (B), and 12 h (C).

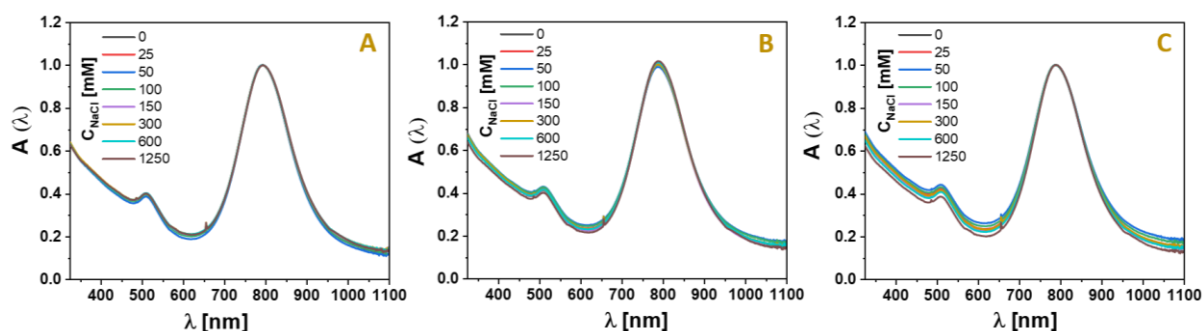


Figure S13. Colloidal stability of GNRs@SiO₂@GNCs plasmophores in NaCl solution of different ionic strength at 0 h (A), 6 h (B), and 12 h (C).

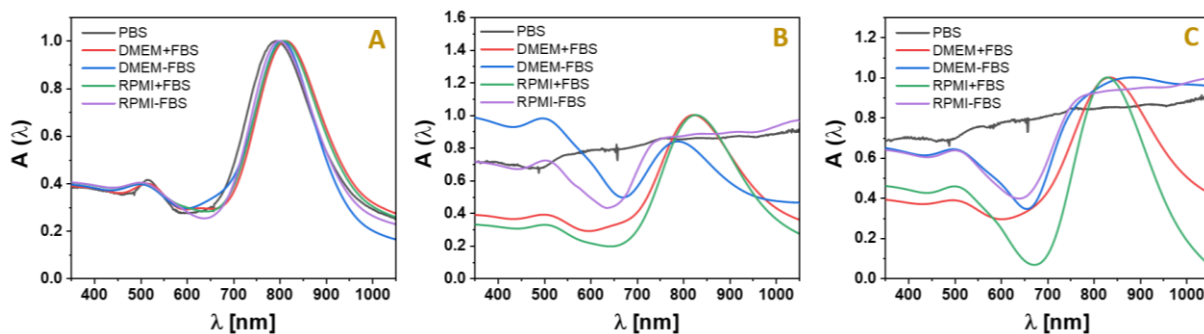


Figure S14. Colloidal stability of GNRs@CTAB in different biological media at 0 h (A), 6 h (B), and 12 h (C).

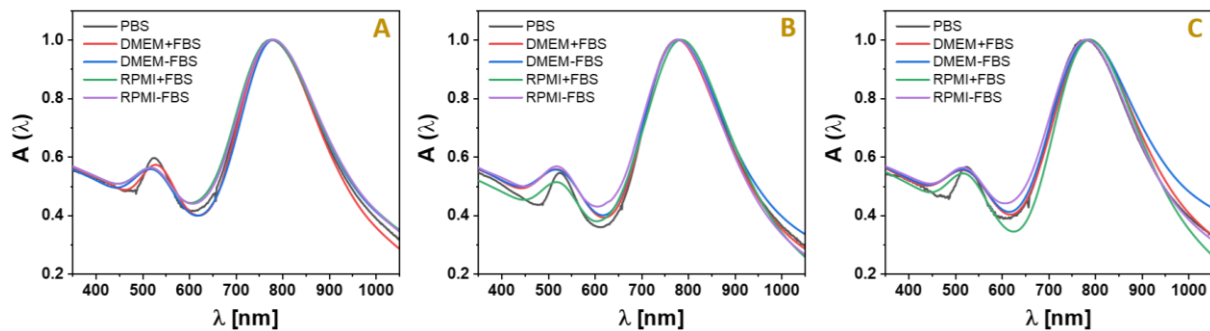


Figure S15. Colloidal stability of GNRs@GNCs in different biological media at 0 h (A), 6 h (B), and 12 h (C).

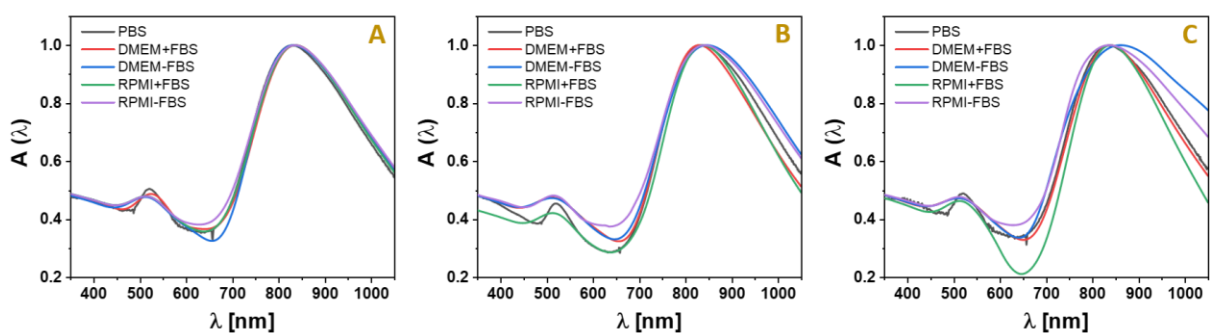


Figure S16. Colloidal stability of GNRs@LBL@GNCs in different biological media at 0 h (A), 6 h (B), and 12 h (C).

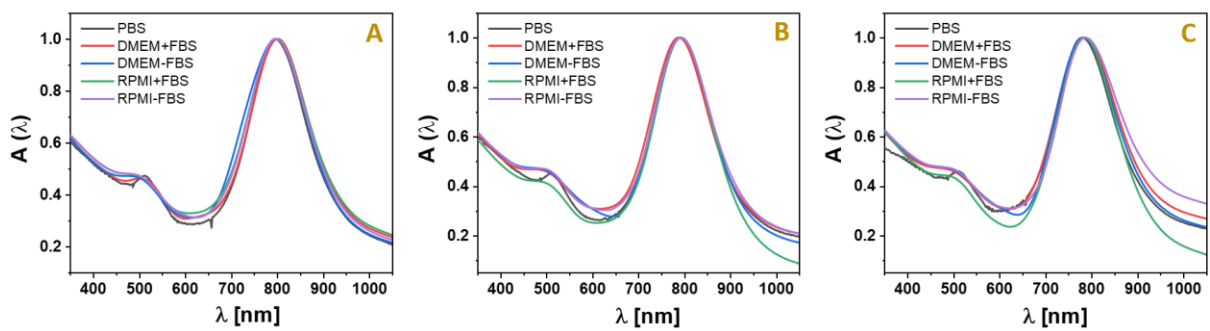


Figure S17. Colloidal stability of GNRs@SiO₂@GNCs plasmaphores in different biological media at 0 h (A), 6 h (B), and 12 h (C).

10. Tuning silica shell thickness of the GNRs@SiO₂@GNCs plasmophores

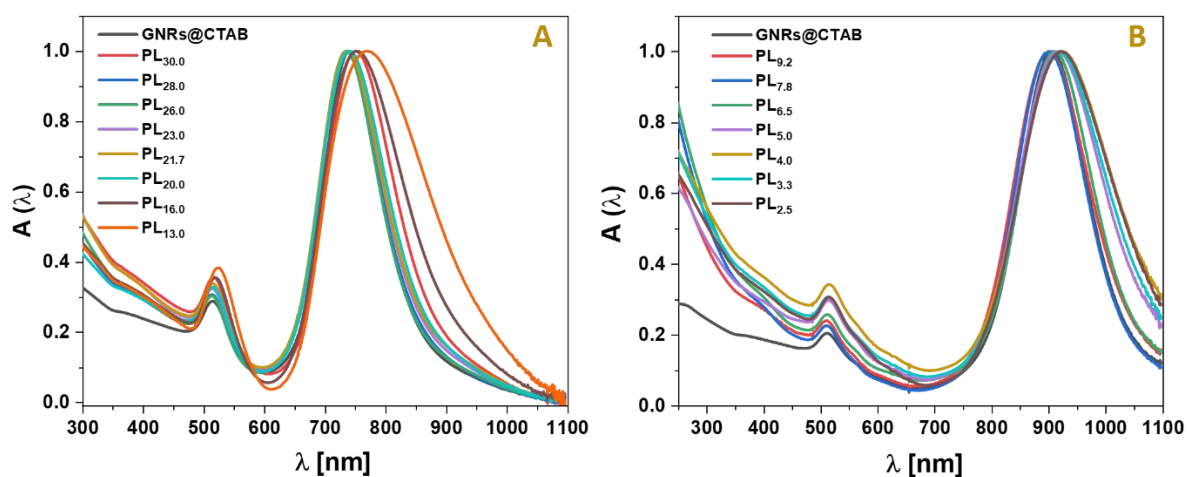


Figure S18. UV-vis absorption spectra of low (A) and high (B) aspect ratio GNRs@SiO₂@GNCs plasmophores of different silica shell thickness (PL= plasmophore, number indicates the thickness of silica shell in nm).

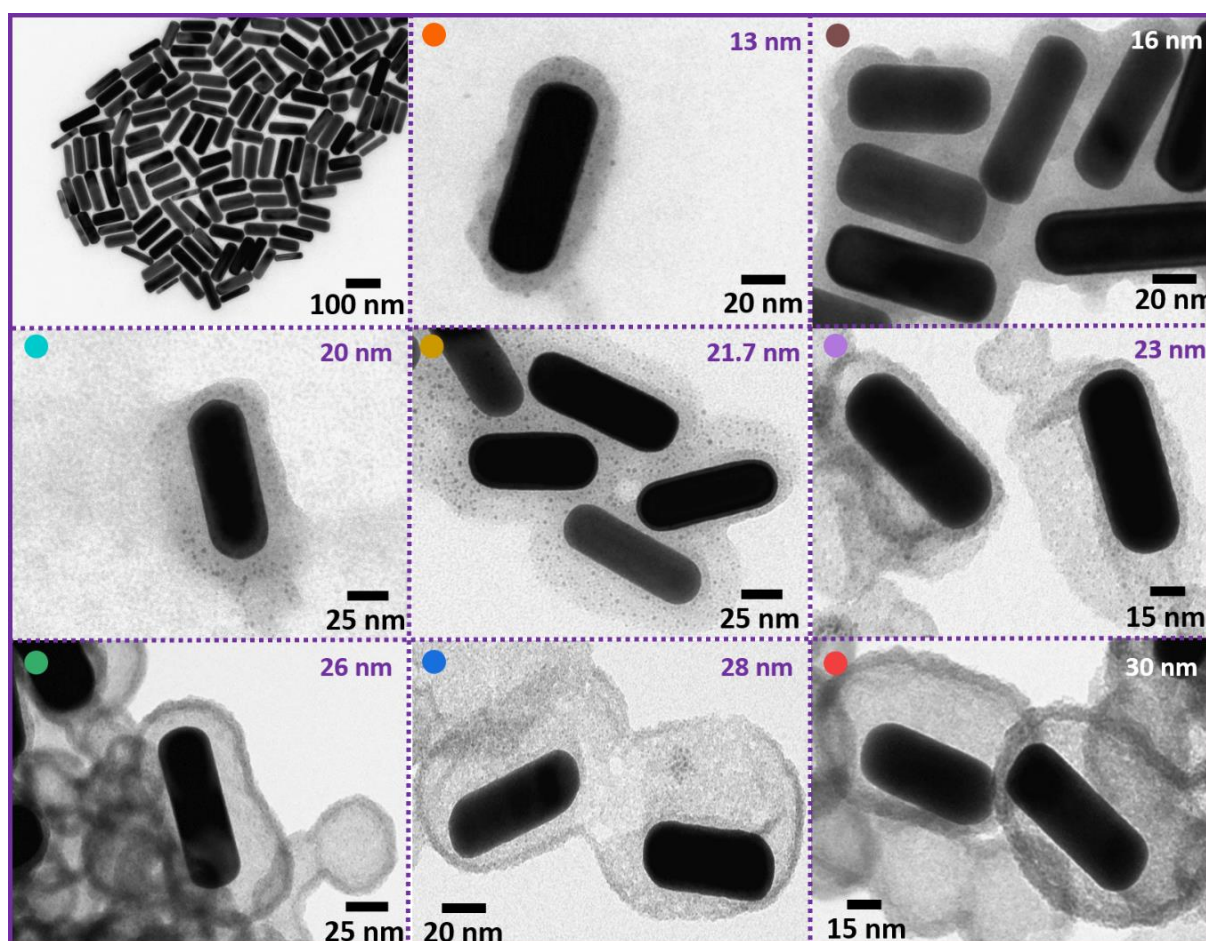


Figure S19. TEM of low aspect ratio GNRs@SiO₂@GNCs plasmophores of different silica shell thickness. Upper panel, left to right (GNRs@CTAB, PL₁₃, PL₁₆). Middle panel, left to right (PL₂₀, PL_{21.7}, PL₂₃), Lower panel, left to right (PL₂₆, PL₂₈, PL₃₀).

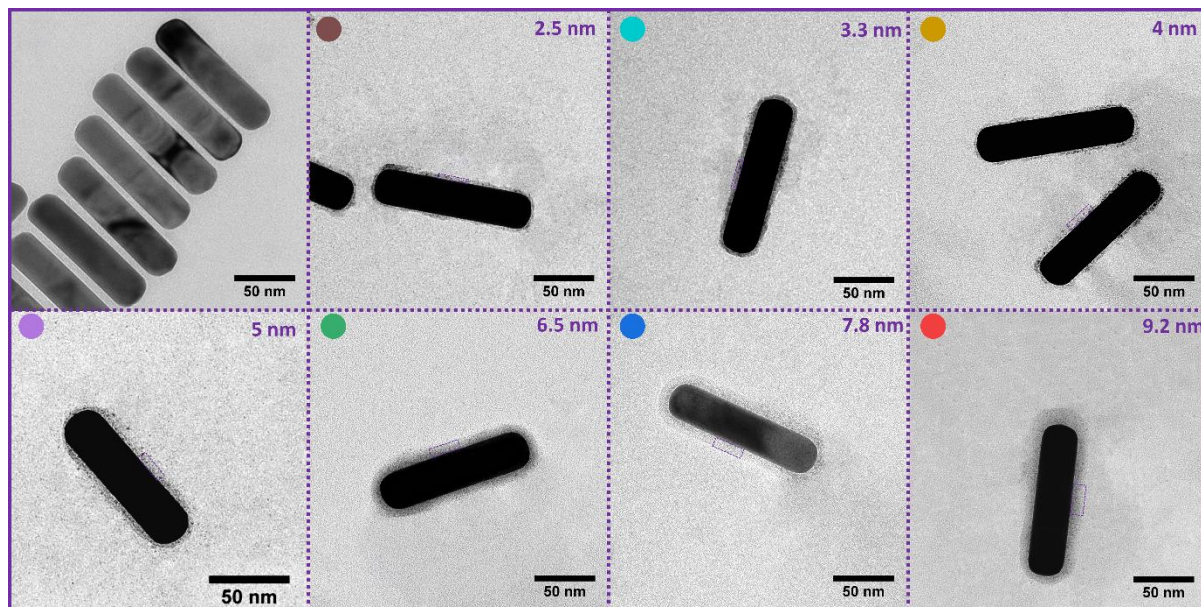


Figure S20. TEM of high aspect ratio GNRs@SiO₂@GNCs plasmophores of different silica shell thickness. Upper panel, left to right (GNRs@CTAB, PL_{2.5}, PL_{3.3}, PL₄). Lower panel, left to right (PL₅, PL_{6.5}, PL_{7.8}, PL_{9.2}).

11. Photophysical properties of the GNRs@SiO₂@GNCs plasmophores

Steady state fluorescence of GNRs@SiO₂@GNCs plasmophores

The distant-dependent fluorescence of both, low and high AR GNRs@SiO₂@GNCs plasmophores synthesized using different thickness of the silica shell dielectric spacer was studied. The CTAB-capped GNRs were firstly overcoated with different SiO₂ thickness (~13 - 30 nm for low AR GNRs, and ~2.5 - 9.2 nm for high AR GNRs) and the resultant GNRs@SiO₂ were subsequently functionalized by the fluorescent GNCs@GSH as described *vide supra*. The resultant GNRs@SiO₂@GNCs plasmophore solutions were then purified by three consecutive centrifugation cycles at 5000 rpm for 45 min to get rid of excess GNCs. The pellets were subsequently redispersed in 2 mL of MQ water and the distance-dependent fluorescence of the plasmophores was then recorded using a spectrofluorometer ($\lambda_{exc} = 365$ nm, $\lambda_{em} = 600$ nm).

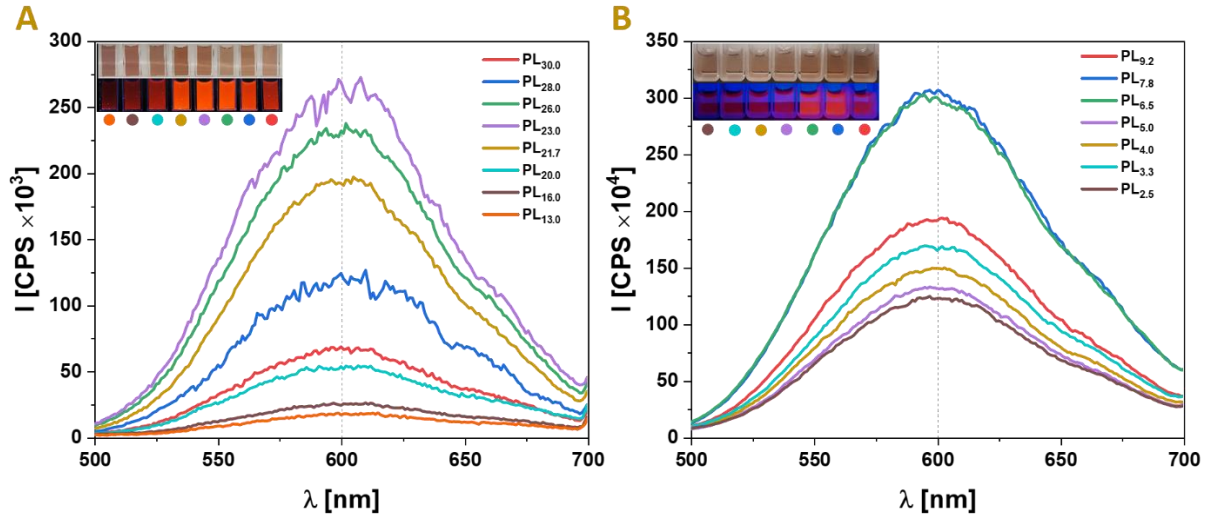


Figure S21. Steady-state fluorescence spectra of low (A) and high (B) aspect ratio GNRs@SiO₂@GNCs plasmophores of different silica shell thickness.

Fluorescence decay measurements of GNRs@SiO₂@GNCs plasmophores

Fluorescence decay curves of the GNRs@SiO₂@GNCs were measured using a Fluotime300, time-correlated single photon counting instrumentation from Picoquant. A blue diode, PDL-800D by Picoquant, (central wavelength: 436 nm) was used for excitation. The pulse repetition rate was adjusted to 62.5 kHz (16 μs between pulses). Scattered excitation light was removed using a longpass filter (cutoff wavelength: 450 nm). Exponential decay fits were performed using the EasyTau2 software by Picoquant. Only data points where the remaining signal was $\geq 1\%$ of the peak signal were taken into account for the fits, since the samples had completely relaxed by then. Fits were accepted when chi-square (χ^2) < 1.3.[16] Tri-exponential decays fits were applied accordingly. Mean lifetimes were calculated as follows[17]:

$$\tau_{ave} = \frac{\sum_i I_i \tau_i}{\sum_i I_i} = \frac{\sum_i A_i \tau_i^2}{\sum_i A_i \tau_i}$$

Where τ_i and I_i and A_i are the corresponding lifetimes, intensities and amplitudes of the i th component of the multi-exponential decay.

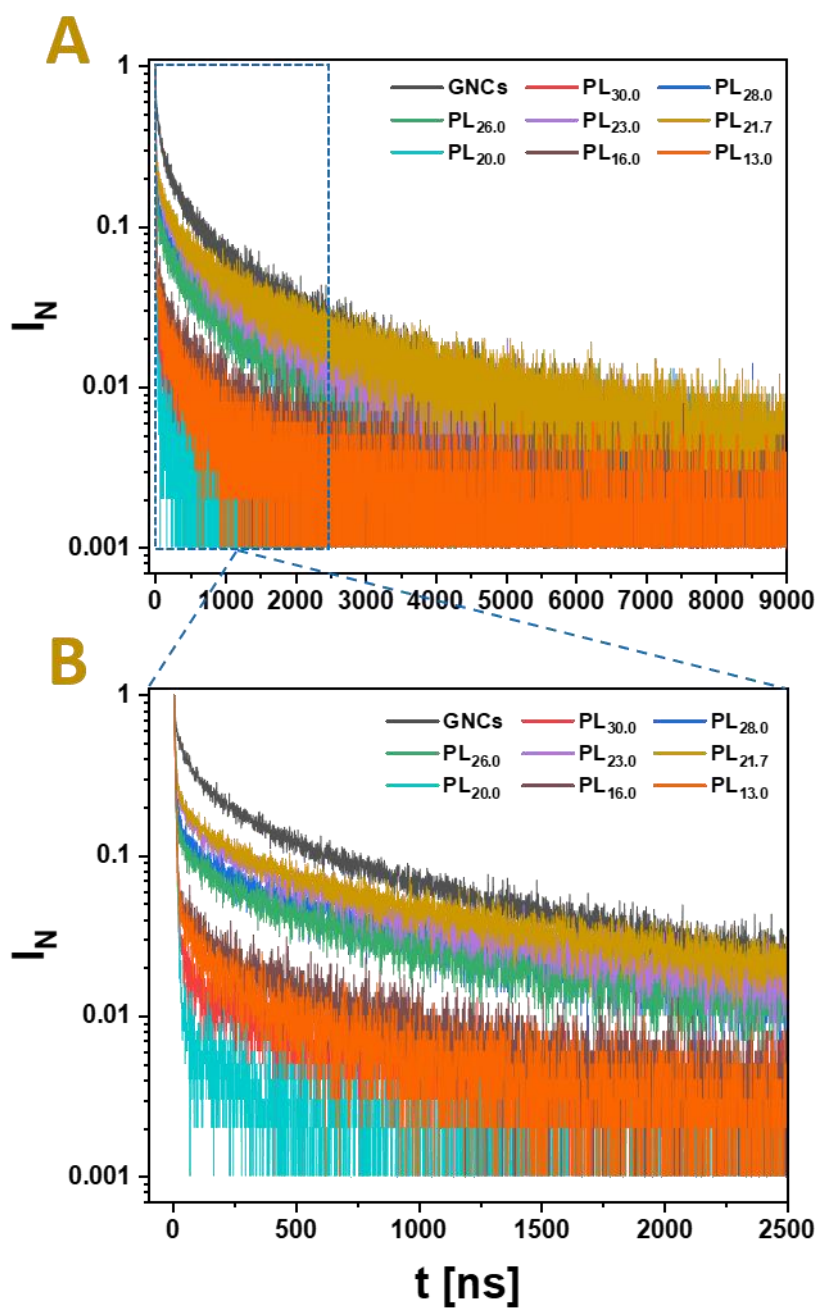


Figure S22. (A) Fluorescence decay curves of GNCs and low aspect ratio GNRs@SiO₂@GNCs plasmaphores of different silica shell thickness. (B) Zoomed-in fluorescence decay curves from squared area in (A).

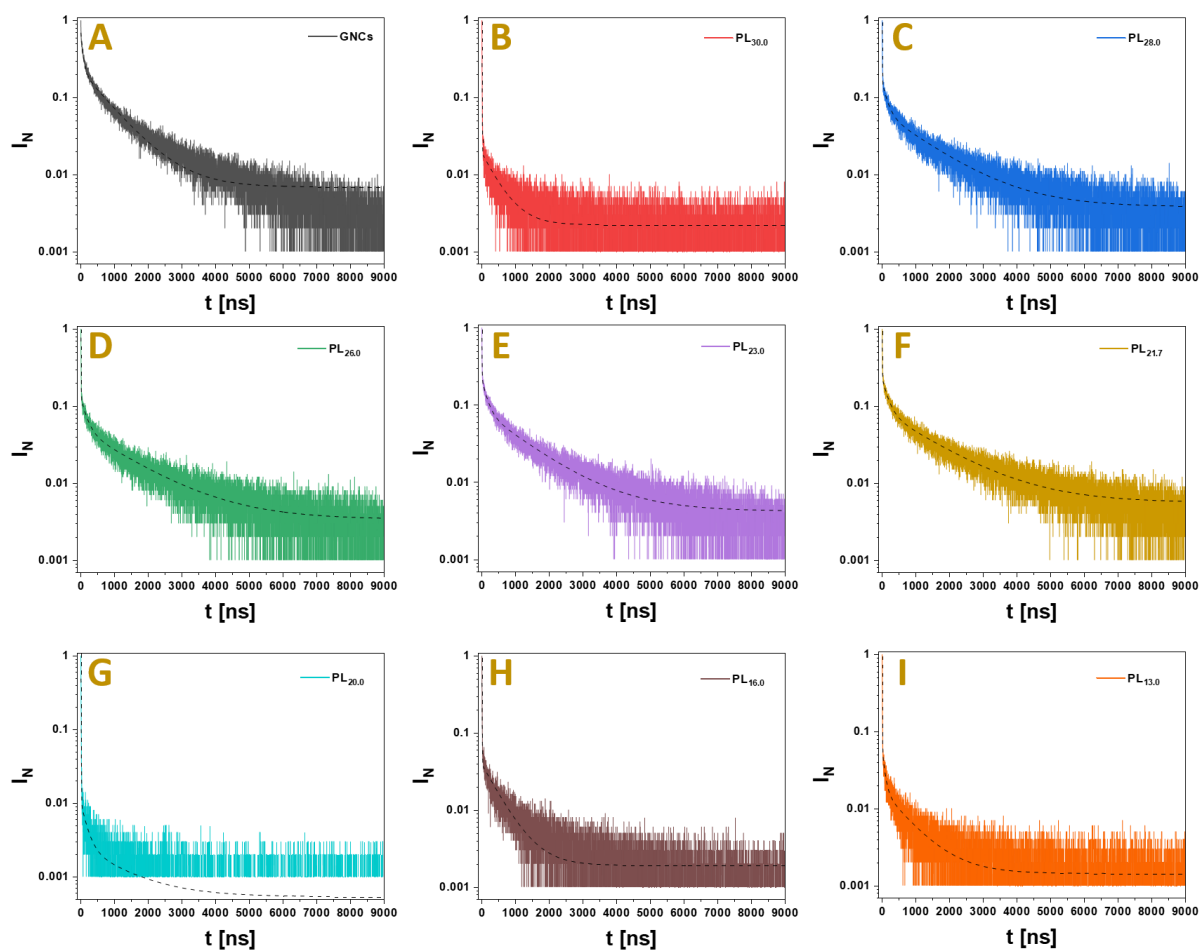


Figure S23. Experimental (solid-colored lines) and fitted (dashed black lines) fluorescence decay curves of GNCs (A) and low aspect ratio GNRs@SiO₂@GNCs plasmophores of different silica shell thicknesses (B-I).

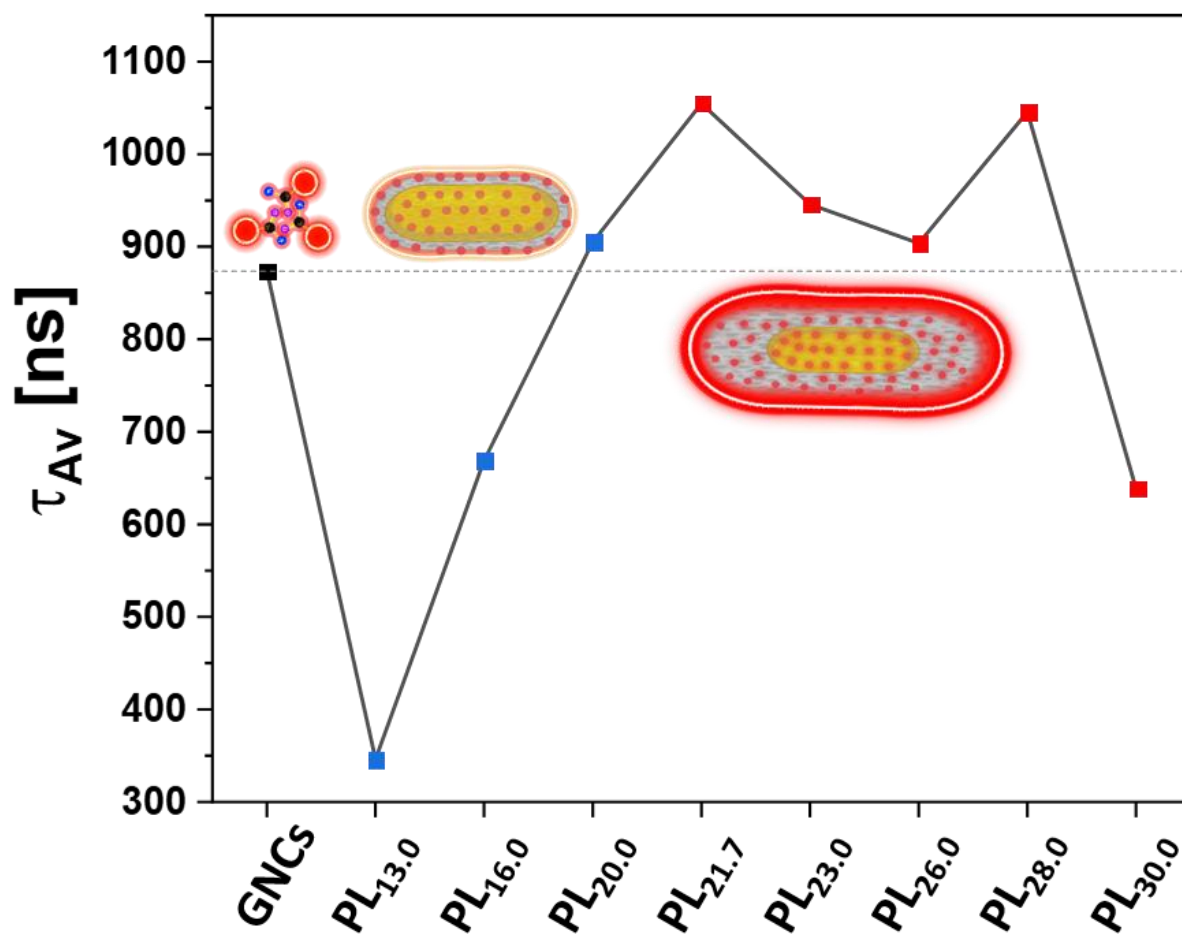


Figure S24. Silica thickness-dependent average fluorescence lifetime (τ_{Av}) of low aspect ratio GNRs@SiO₂@GNCs plasmophores compared to free GNCs (Insets are cartoon illustrations of GNCs, thin and thick plasmophores).

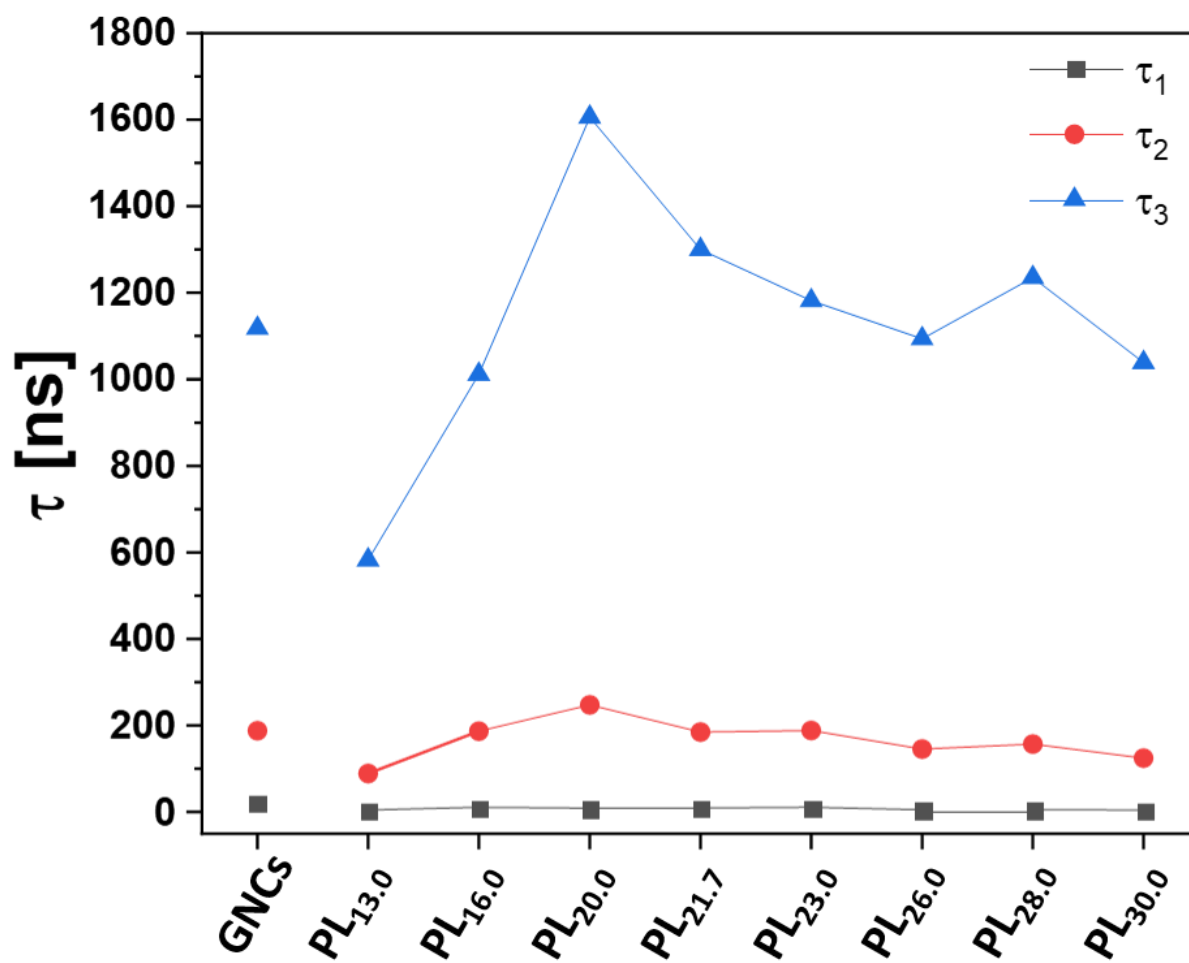


Figure S25. Fluorescence lifetime components of low aspect ratio GNRs@SiO₂@GNCs plasmophores of different silica shell thickness compared to free GNCs. τ_1 , τ_2 , and τ_3 are the short, intermediate, and long fluorescence lifetime components, respectively.

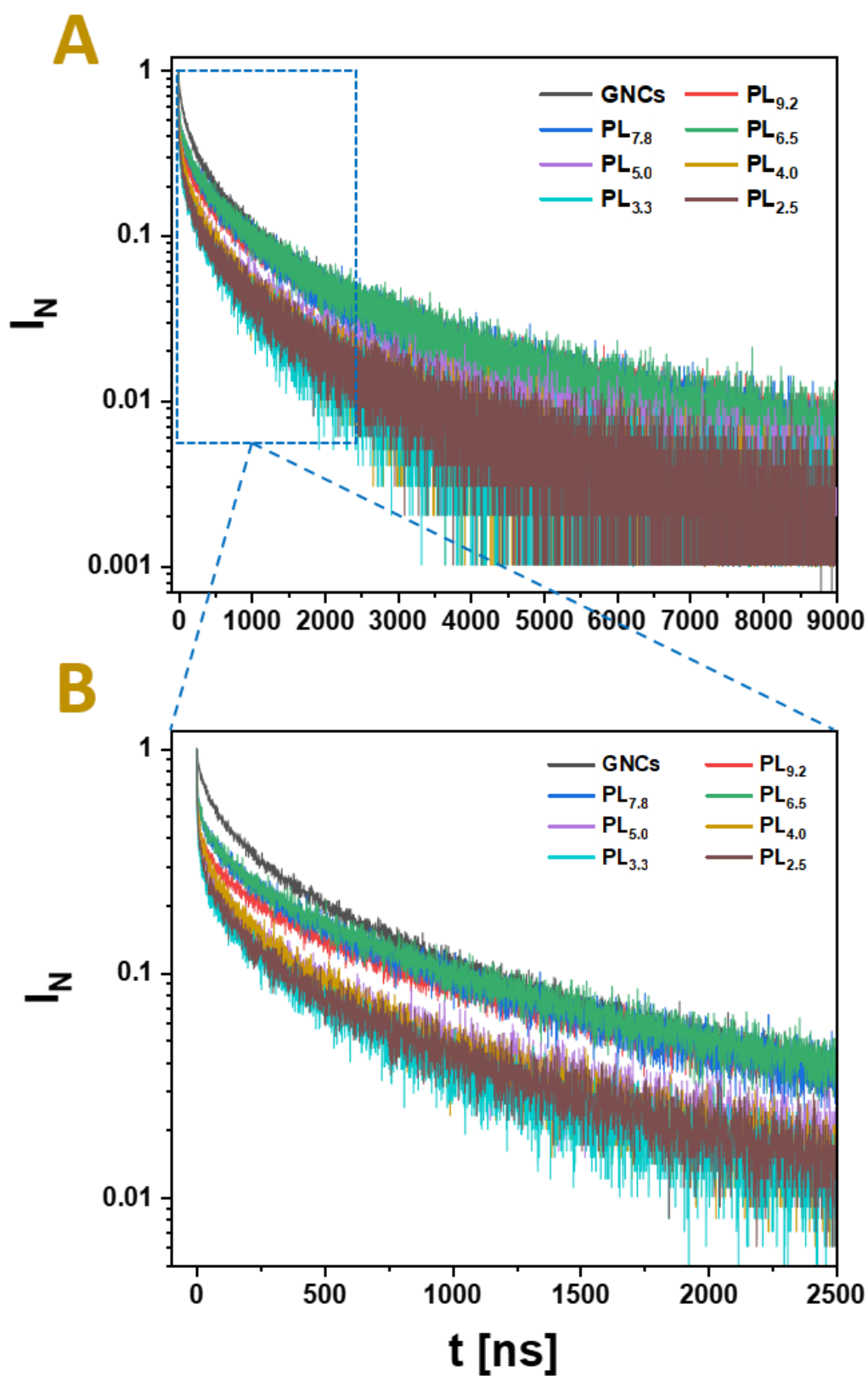


Figure S26. (A) Fluorescence decay curves of GNCs and high aspect ratio GNRs@SiO₂@GNCs plasmophores of different silica shell thickness. (B) Zoomed-in fluorescence decay curves from squared area in (A).

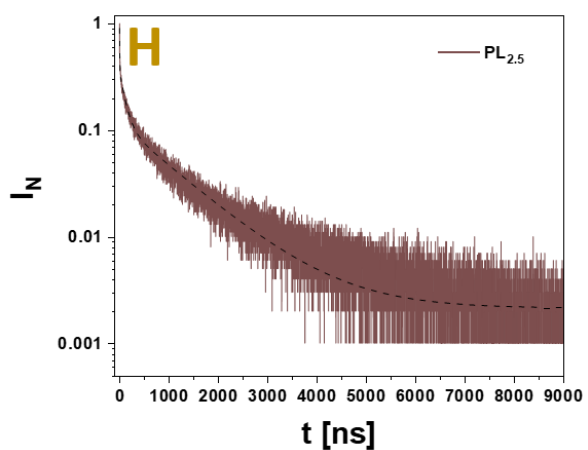
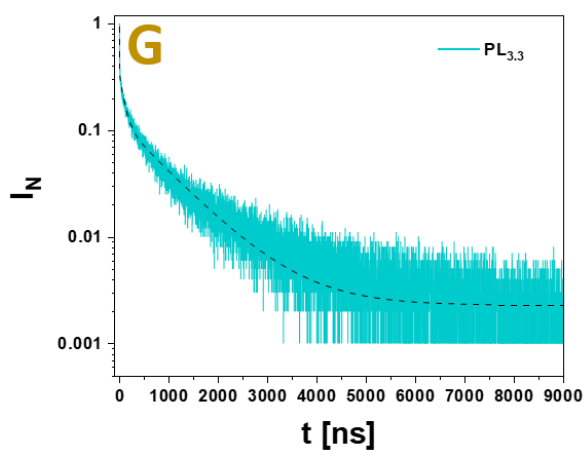
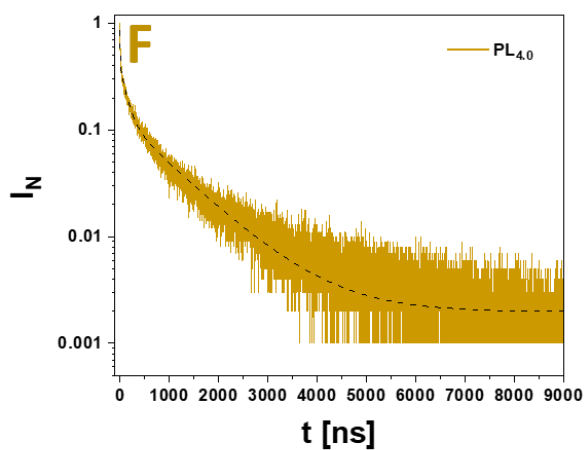
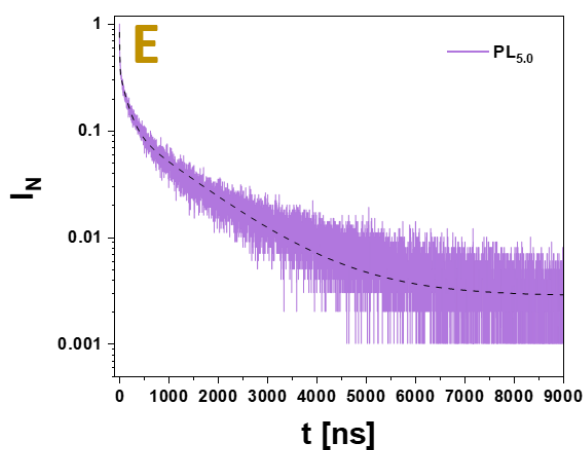
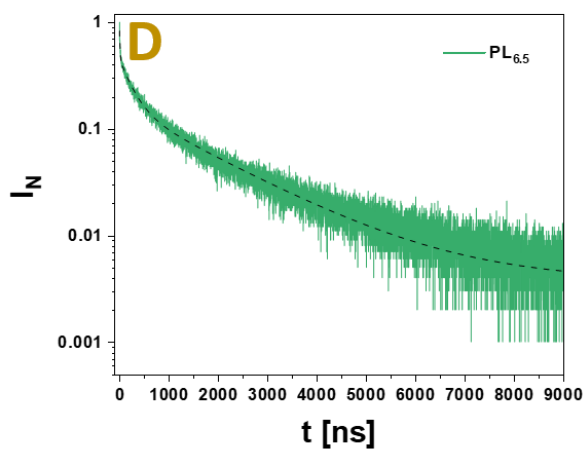
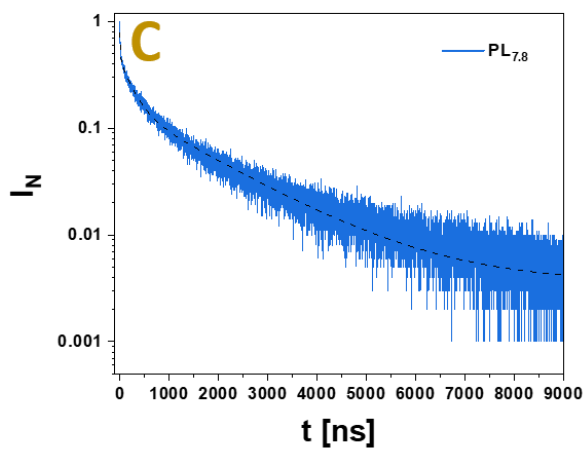
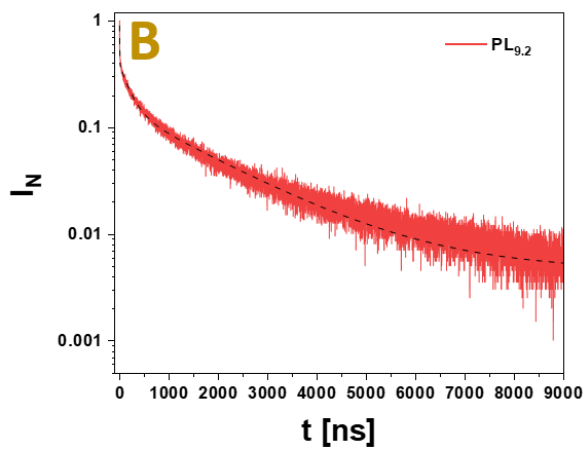
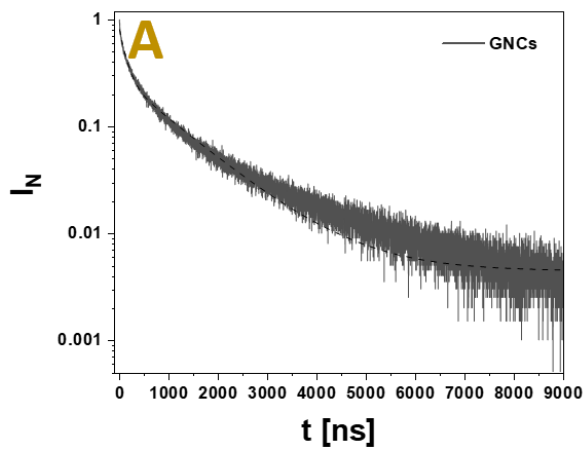


Figure S27. Experimental (solid colored lines) and fitted (dashed black lines) fluorescence decay curves of GNCs (A) and low aspect ratio GNRs@SiO₂@GNCs plasmophores of different silica shell thickness (B-H).

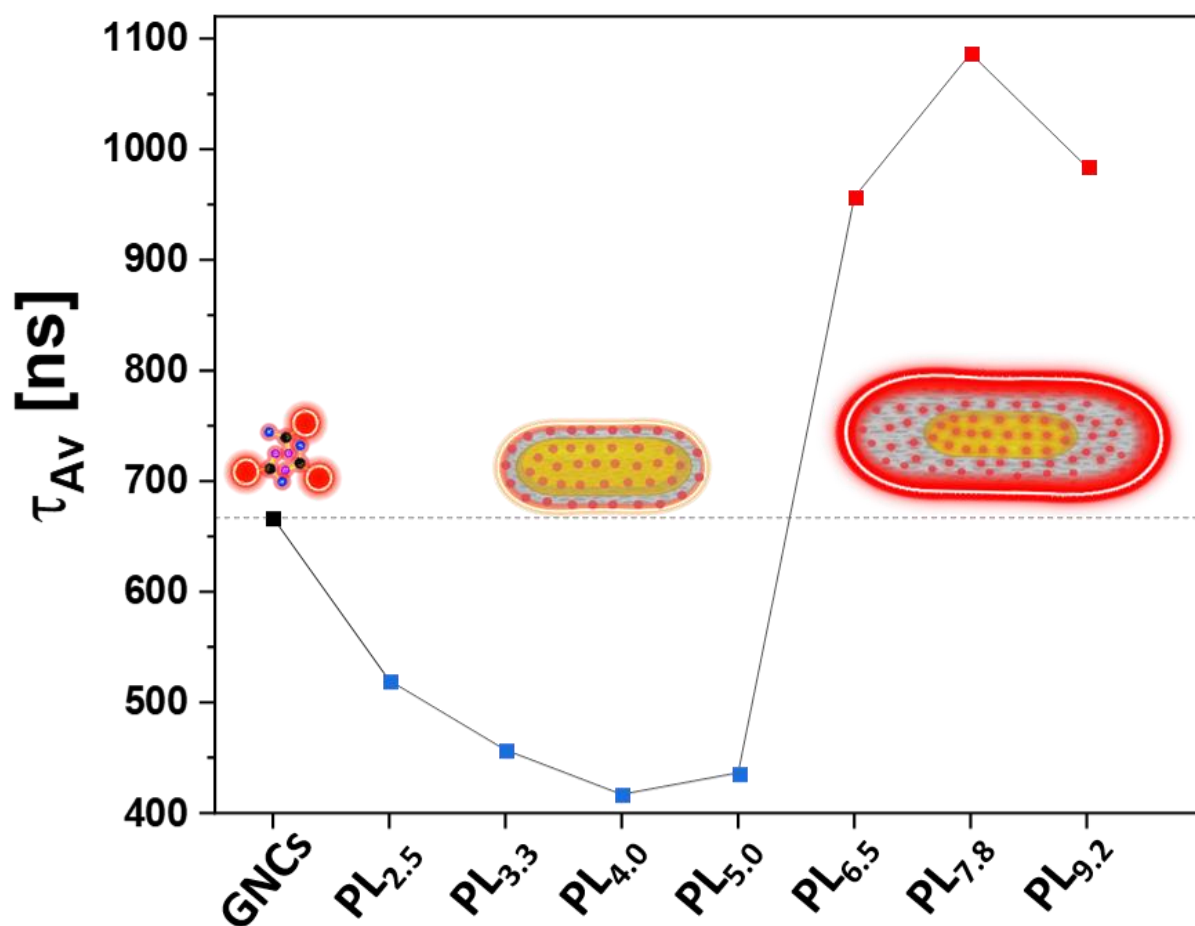


Figure S28. Silica thickness-dependent average fluorescence lifetime (τ_{Av}) of high aspect ratio GNRs@SiO₂@GNCs plasmophores compared to free GNCs (Insets are cartoon illustrations of GNCs, thin and thick plasmophores).

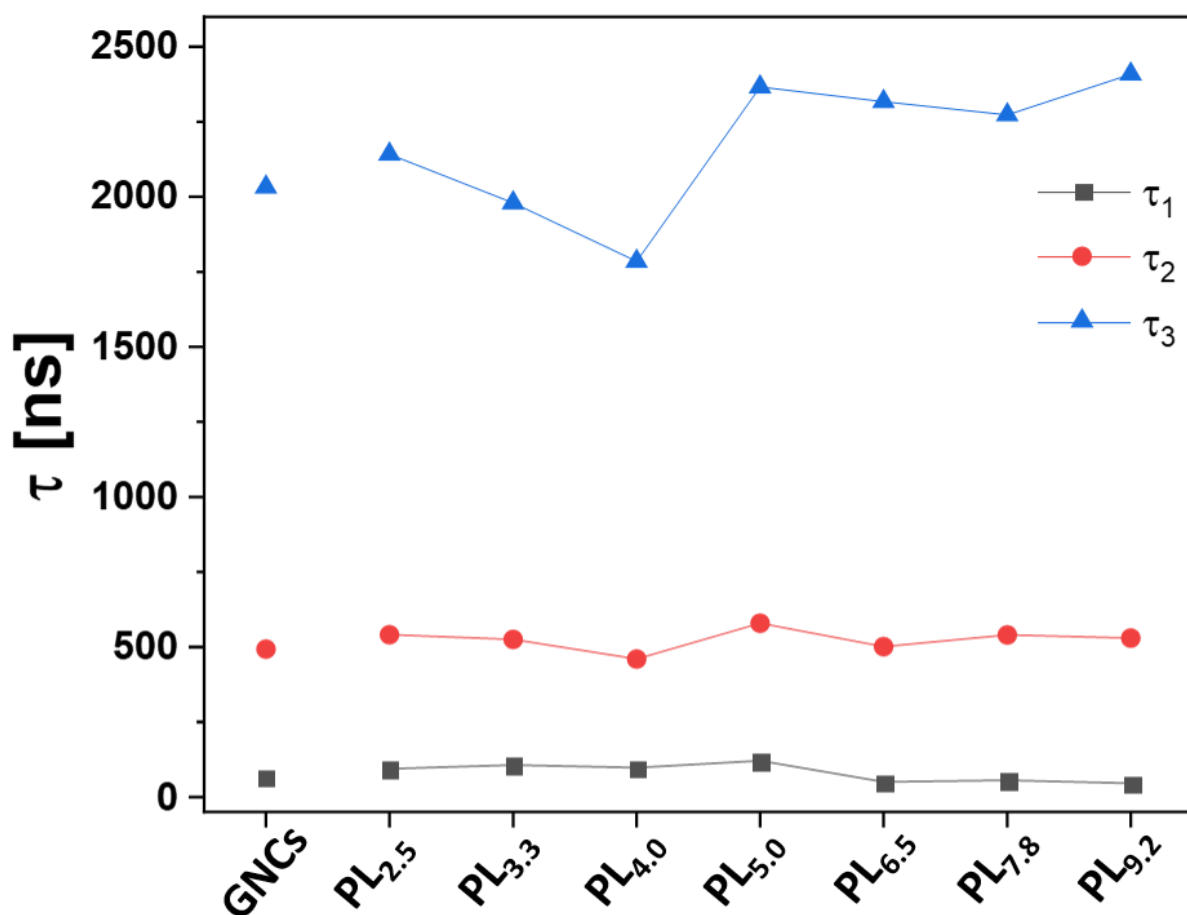


Figure S29. Fluorescence lifetime components of high aspect ratio GNRs@SiO₂@GNCs plasmophores of different silica shell thickness compared to free GNCs. τ_1 , τ_2 , and τ_3 are the short, intermediate, and long fluorescence lifetime components, respectively.

Calculating QY (ϕ), radiative decay constant (K_R) and non-radiative decay constant (K_{NR}) of GNRs@SiO₂@GNCs plasmophores

The relative quantum yield (QY) (ϕ) of GNCs@GSH and GNRs@SiO₂@GNCs plasmophores was determined by comparing their fluorescence efficiency to the fluorescence efficiency of a standard fluorophore using the following equation[18]:

$$\phi_x = \phi_{St} \left(\frac{Grad_x}{Grad_{St}} \right) \left(\frac{\eta_x}{\eta_{St}} \right)^2 \quad (1)$$

Where ϕ is the fluorescence quantum yield, Grad is the gradient value obtained by plotting the integrated area under the emission curve of test/standard samples with respect to their

corresponding absorbance values at the excitation wavelength, η is the refractive index of the used solvents, and the subscripts x and St refer to the test samples (GNCs and plasmophore) and standard (quinine sulfate).

Firstly, the optical density of different concentrations of test samples and standard solution were recorded at λ_{365} using an UV-vis absorption spectrometer. The emission spectra of these solutions were subsequently recorded using a spectrofluorometer at the excitation wavelength $\lambda_{exc} = 365$ nm. The area under the curves of the emission spectra (I_I) of each sample was calculated and was plotted against their corresponding absorbance and the Grad values of test/standard samples was determined thereof. The ϕ values of GNCs and plasmophore were determined using **eq. 1**.

The radiative decay (K_R) and non-radiative decay (K_{NR}) of GNCs and plasmophore could be also calculated from their ϕ values using **eq. 2** and **eq.3** as follows:

$$\phi = \tau_{Av} \times K_R \quad (2)$$

$$\phi = \frac{K_R}{K_R + K_{NR}} \quad (3)$$

Where τ_{Av} is the average photoluminescence lifetime.

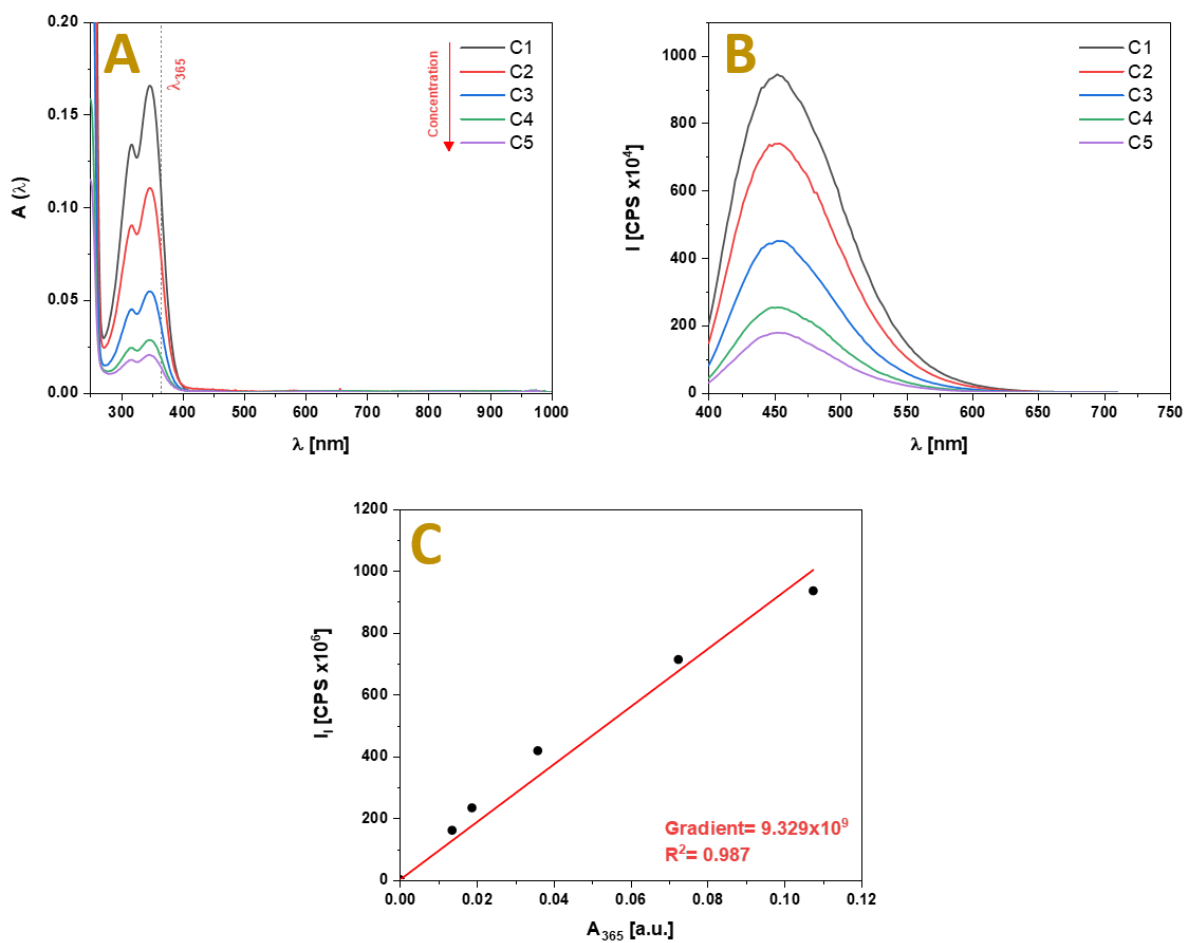


Figure S30. Calculating the gradient of integrated fluorescence intensity vs. optical density of the standard fluorophore (Quinine sulfate). (A) UV-vis absorption spectra and (B) PL spectra of different concentration of quinine sulfate, and (C) plot of integrated fluorescence intensity (I_f) vs. optical density of different concentration of quinine sulfate standard solutions at $\lambda = 365$ nm (A_{365}).

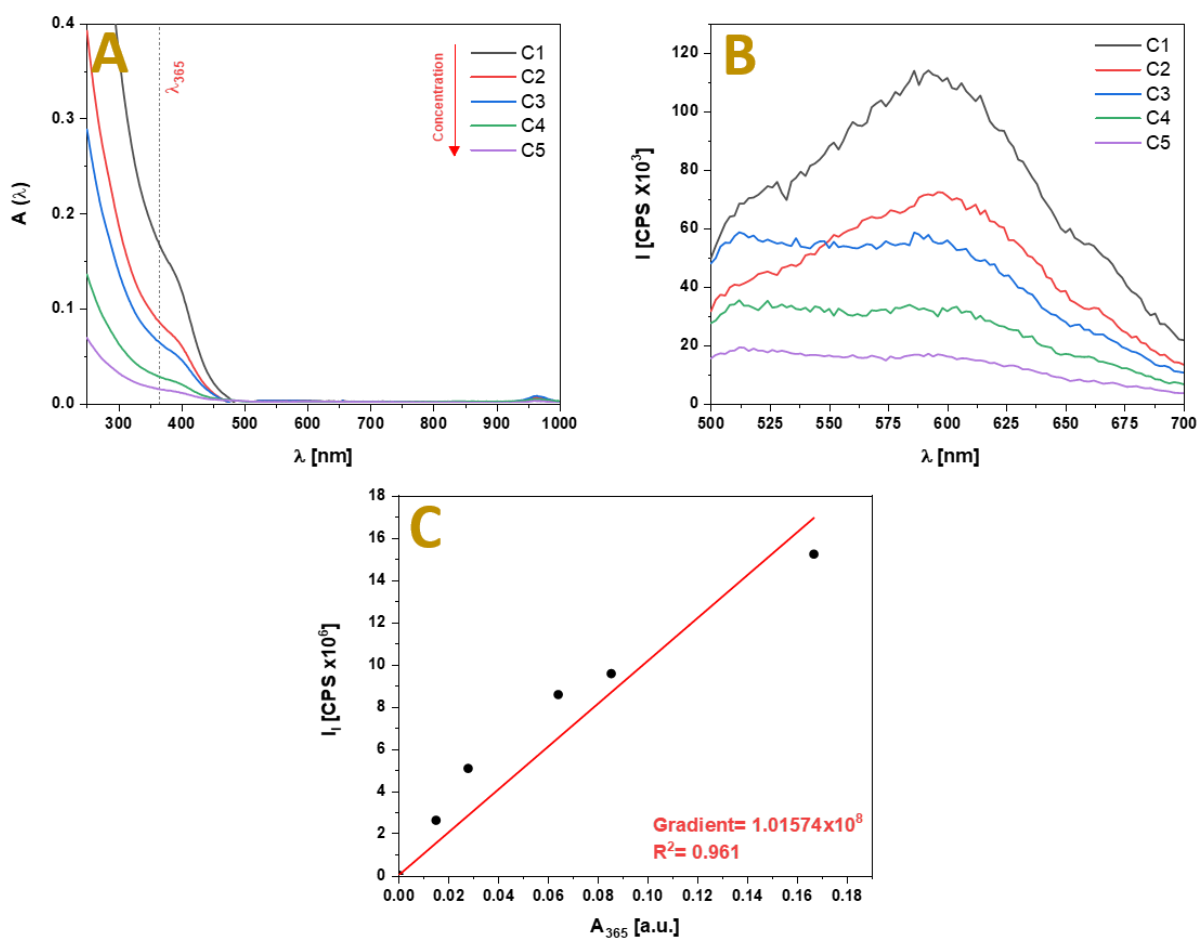


Figure S31. Calculating the gradient of integrated fluorescence intensity vs. optical density of GNCs. (A) UV-vis absorption spectra and (B) PL spectra of different concentration of GNCs, and (C) plot of integrated fluorescence intensity (I_i) vs. optical density of different concentration of GNCs solutions at $\lambda = 365$ nm (A_{365}).

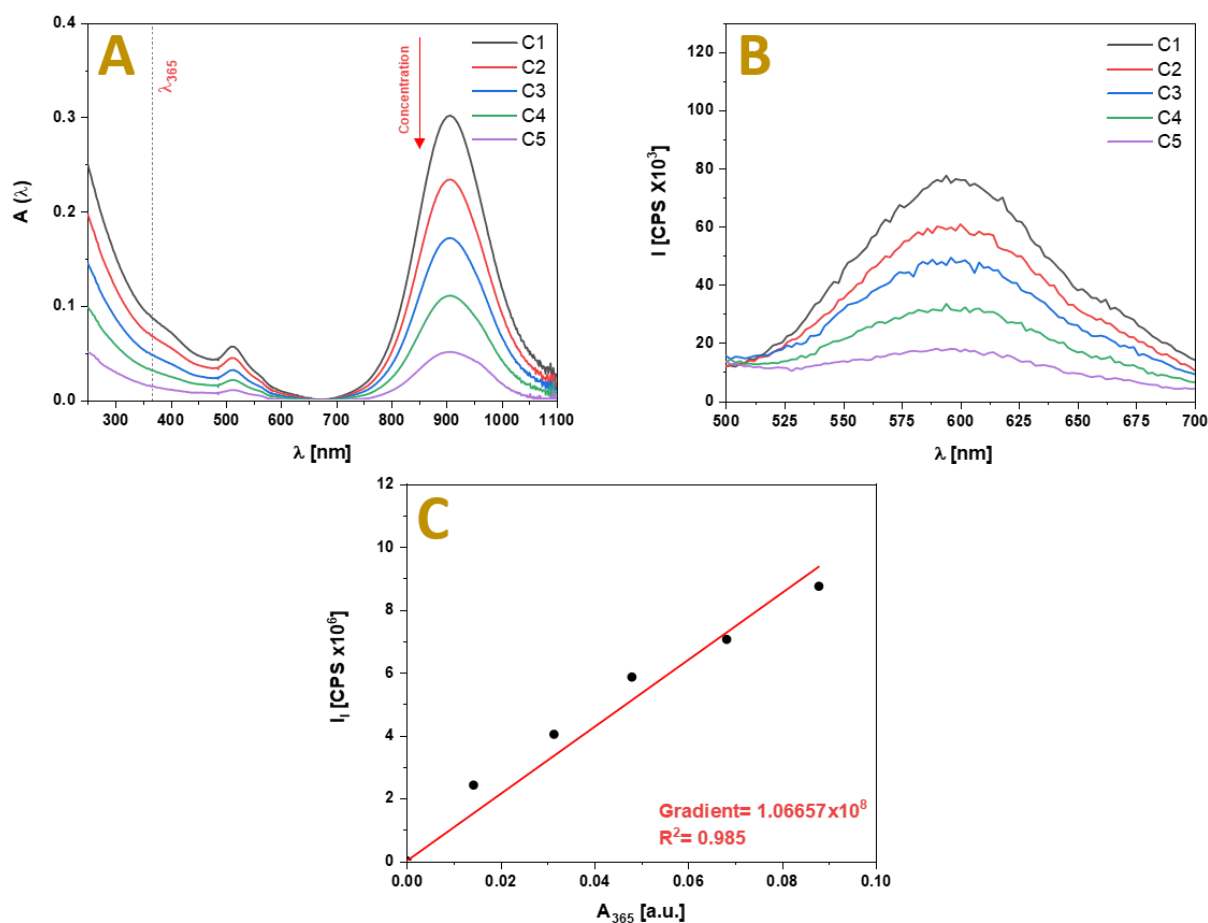


Figure S32. Calculating the gradient of integrated fluorescence intensity vs. optical density of Plasmophore (high aspect ratio GNRs@Si2@GNCs plasmophore). (A) UV-vis absorption spectra and (B) PL spectra of different concentration of GNRs@Si2@GNCs plasmophore, and (C) plot of integrated fluorescence intensity (I_1) vs. optical density of different concentration of GNRs@Si2@GNCs plasmophore solutions at $\lambda = 365$ nm (A_{365}).

Table S1. QY (ϕ), radiative decay constant (K_R) and non-radiative decay constant (K_{NR}) of GNCs and plasmophores (high aspect ratio GNRs@Si2@GNCs plasmophores).

Sample	Gradient	η	Φ [%]	τ_{Av} [ns]	K_R [s^{-1}]	K_{NR} [s^{-1}]	K_R/K_{NR}
Quinine sulfate standard	9.33×10^9	1.3	54.6	N/A	N/A	N/A	N/A
GNCs	1.02×10^8		0.594	667	8.9×10^5	6.1×10^5	1.47
Plasmophores	1.07×10^8		0.624	1087	5.7×10^5	3.4×10^5	1.66

12. Thermal stability of GNRs@CTAB, GNRs@SiO₂, and GNRs@SiO₂@GNCs plasmaphores

In order to study the effect of coating CTAB-capped GNRs with a silica shell in the GNRs@SiO₂ as well as with silica and GNCs in the GNRs@SiO₂@GNCs plasmaphores on their thermal stability at different annealing temperatures, in situ TEM heating as well as solution-based thermal heating experiments were carried out.

In situ TEM heating

The in situ TEM heating was carried out using a TEM facility equipped with a high-temperature specimen stage. During the experiment, the NPs were annealed at different temperatures (25-1000 °C) during which the real-time imaging of heating-induced morphological and structural changes of both, plasmonic cores and GNCs in the GNRs@CTAB, GNRs@SiO₂, and GNRs@SiO₂@GNCs, respectively, after approx. 60 min dwell time at a given temperature was carried out.

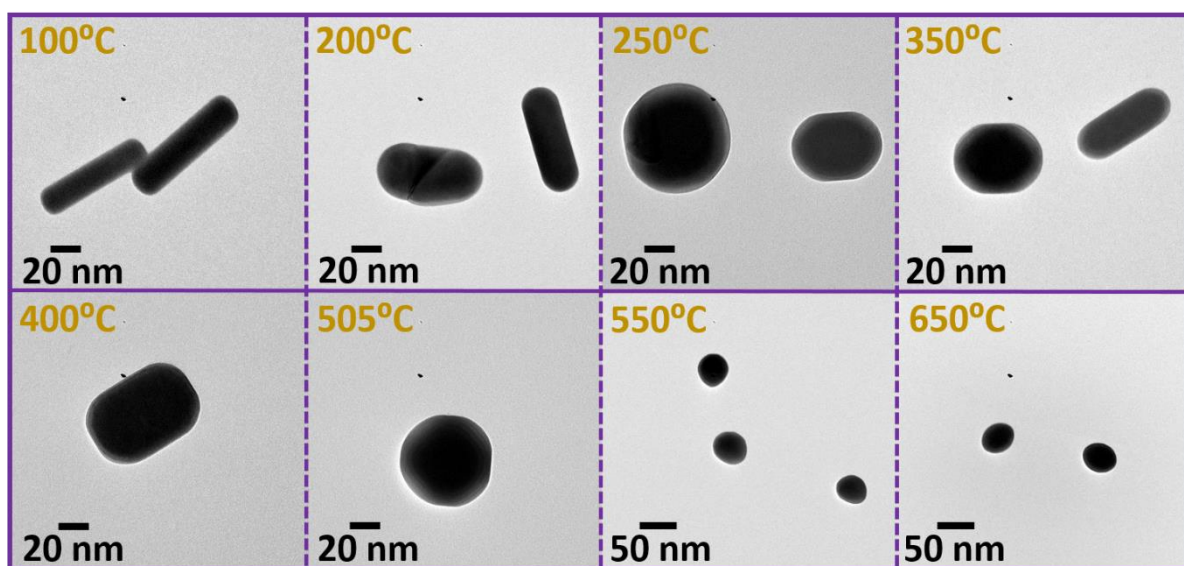


Figure S33. In situ heating TEM study. Thermal annealing of GNRs@CTAB at different annealing temperatures.

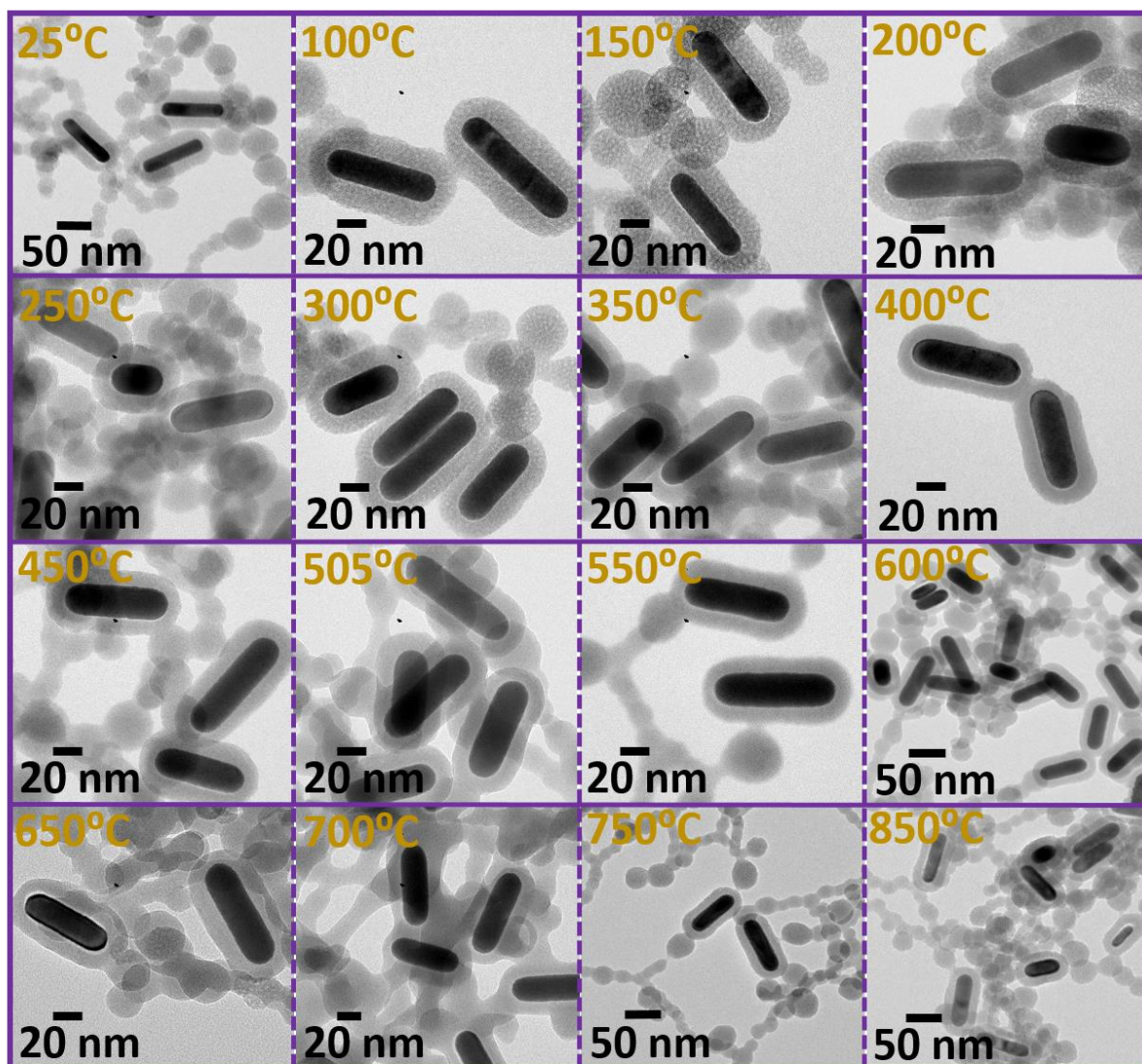


Figure S34. In situ heating TEM study. Thermal annealing of GNRs@SiO₂ at different annealing temperatures.

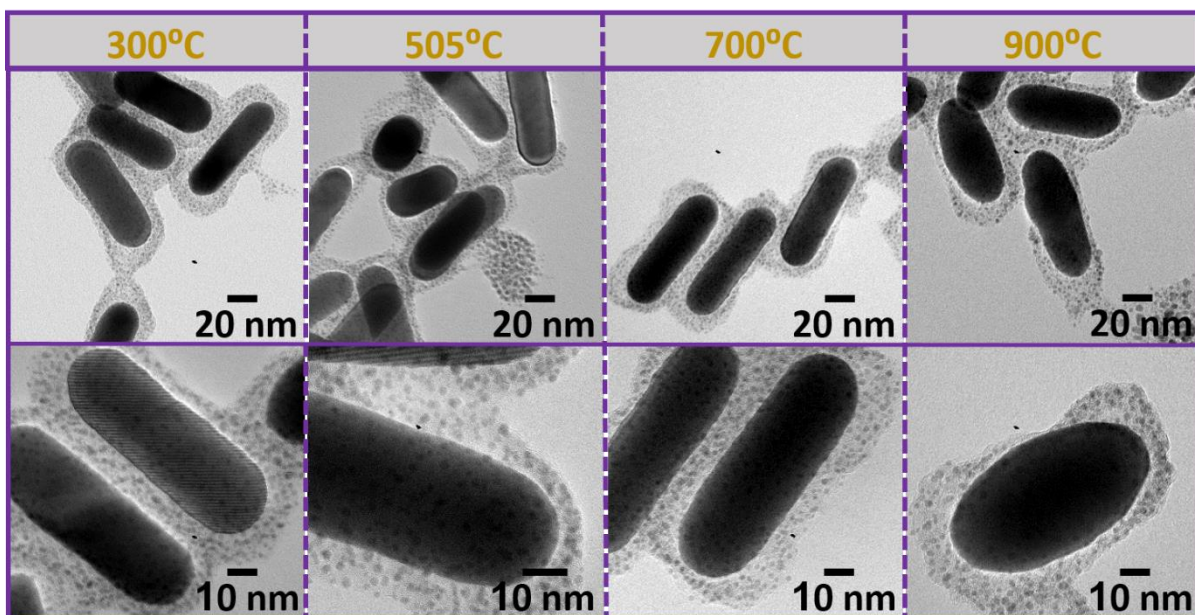


Figure S35. In situ heating TEM study. Low (upper panel) and high (lower panel) magnification TEM micrographs of GNRs@SiO₂@GNCs plasmaphores thermally annealed at different temperatures.

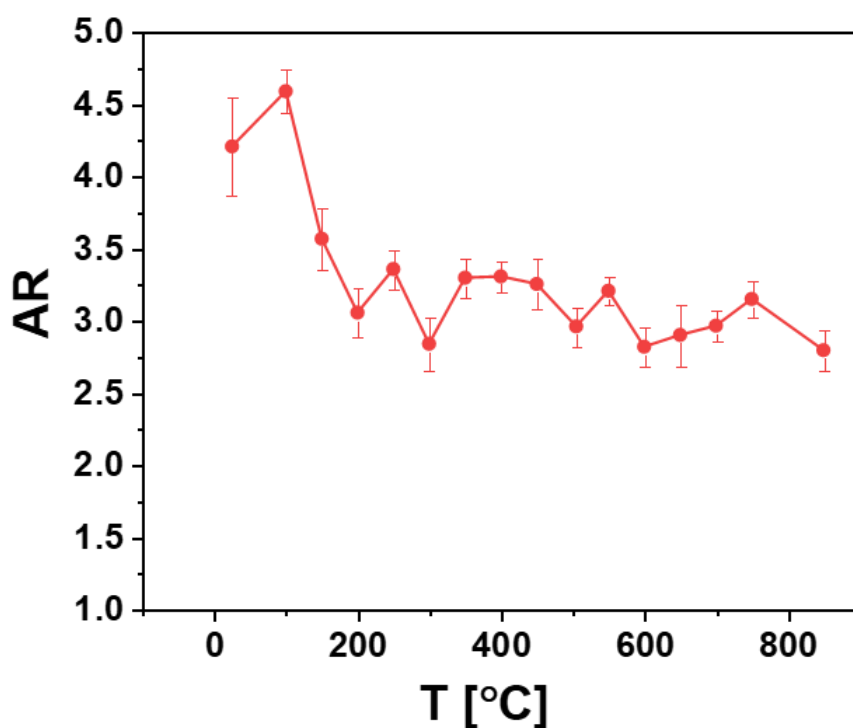


Figure S36. Effect of thermal annealing on the AR of GNRs@SiO₂.

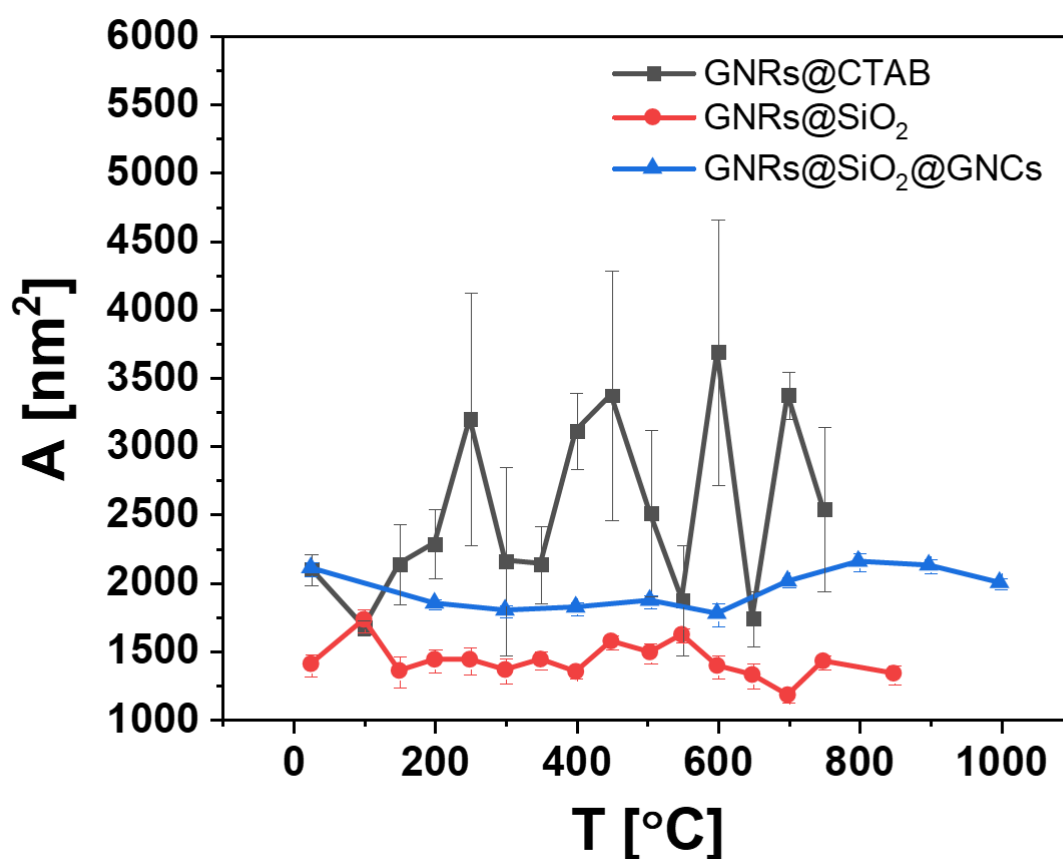


Figure S37. Effect of thermal annealing on the cross-section area of GNRs@CTAB, GNRs@SiO₂, and GNRs@SiO₂@GNCs plasmophores.

Solution-based thermal heating

The thermal stability of GNRs, GNCs, and plasmophores was assessed by recording their UV-vis absorption as well as their PL spectra before and after annealing their solutions at elevated temperature. In a 20 mL scintillation vial, 3 mL of GNRs, GNCs, or plasmophores were transferred and heated to 100 °C and kept for 30 min under moderate stirring. The UV-vis absorption and PL spectra were subsequently recorded using an UV-vis spectrophotometer and spectrofluorometer, respectively. The UV-vis data showed a blue-shift of the LSPR peak of the GNRs upon annealing at 100 °C, whereas, no obvious change in the LSPR peak position for plasmophores. These results are consistent with the solid-state in situ TEM heating experiment. On the other hand, the PL data shows no difference between the PL stability of GNCs and plasmophores upon annealing at 100 °C.

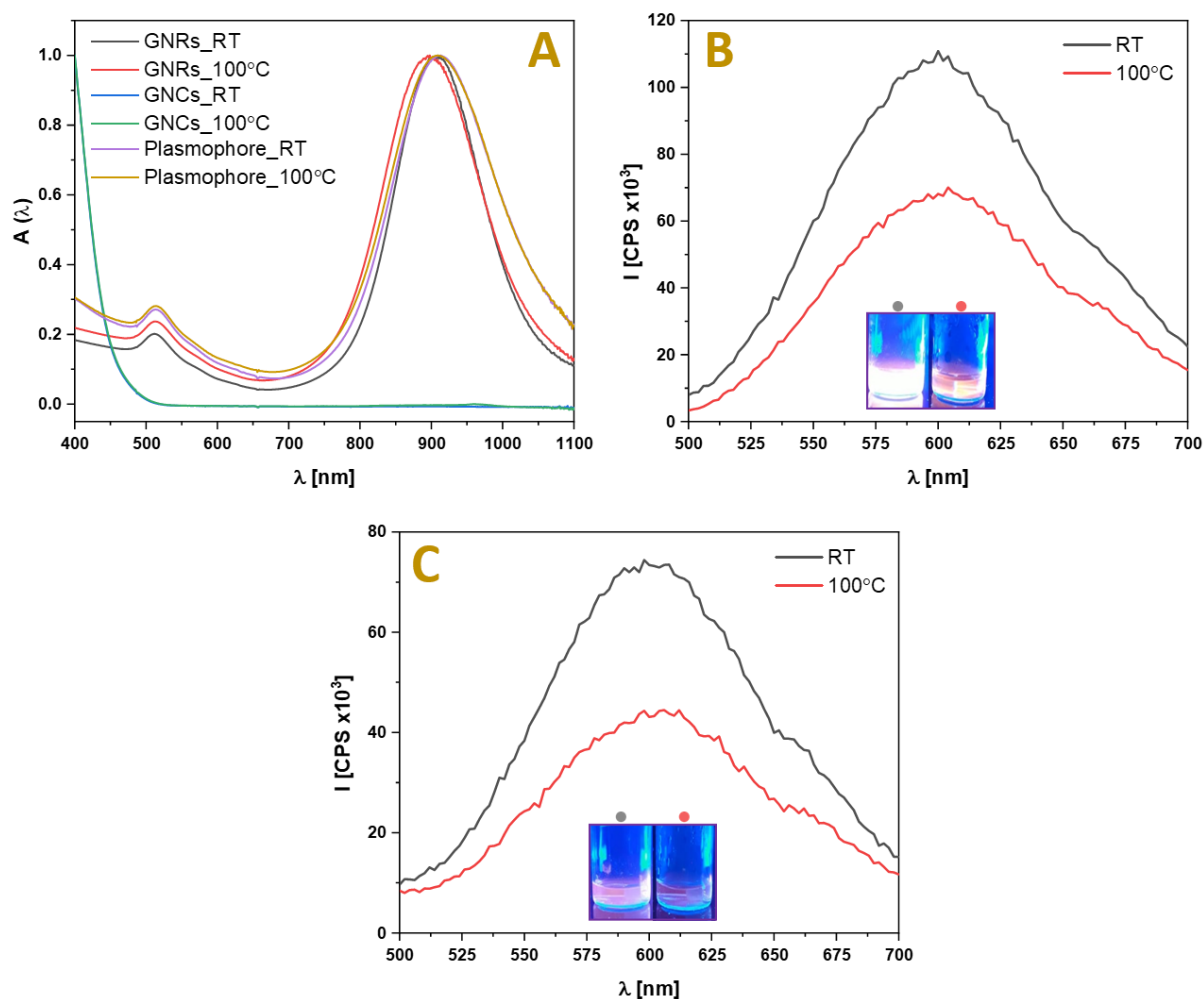


Figure S38. Solution-based thermal heating study. (A) UV-vis absorption spectra of GNRs@CTAB, GNCs, and plasmophores before (room temperature; RT) and after annealing at 100 °C. (B and C) PL spectra of GNCs and plasmophores, respectively, before and after annealing at 100 °C, insets are their corresponding photographs under UV-lamp excitation.

13. Photothermal stability of GNRs@CTAB, GNRs@SiO₂, and GNRs@SiO₂@GNCs plasmophores

The photothermal stability of GNRs in the GNRs@CTAB, GNRs@SiO₂, and GNRs@SiO₂@GNCs plasmophores was studied by evaluating their UV-vis spectral absorption changes as well as their TEM morphological and structural changes upon irradiation with nanosecond (ns) laser pulses. For that, GNRs of different AR (AR~3.5 and 5.5, $\lambda_{\text{LSPR}} = 785$ nm and 900, respectively) and different silica thickness (Si₂₂ and Si₁₅, numbers indicate silica thickness in nm) were used during this study. In brief, 0.5 mL of each sample was transferred into an 1 cm quartz cuvette and was then irradiated with ns laser pulses while stirring to ensure the homogeneous irradiation of all the NPs in the

samples. The laser irradiation of NPs was carried out using Nd:YAG ns-laser source (Innolas, SpitLight DPSS250-100) with a pulse width of 9 ns at a wavelength of 1064 nm. The pulse repetition rate was set at 100 Hz, which produced a pulse energy of 10 mJ and total energy fluence per pulse of 320 mJ/cm². In this experiment, the NPs were irradiated with an average of 200-9000 ns-laser pulses. Shortly after that, changes in the UV-vis absorption spectra were recorded using UV-vis spectroscopy and the morphological and structural changes were assessed using TEM imaging. To assess the photothermal stability of the conjugated GNCs, the fluorescence behavior of GNRs@SiO₂@GNCs plasmophores was evaluated using spectrofluorometry and under UV lamp excitation after their irradiation with the ns-laser pulses.

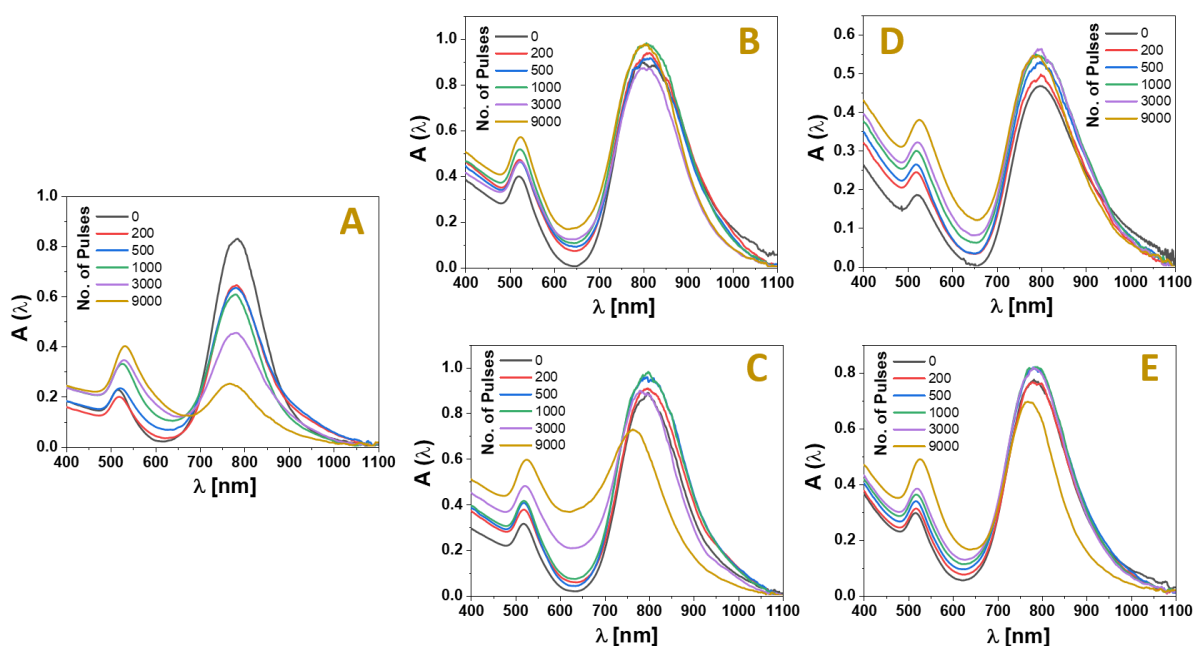


Figure S39. Photothermal-mediated reshaping of low AR GNRs@SiO₂@GNCs plasmophores. UV-vis absorption spectra of GNRs@CTAB (A), different silica thickness GNRs@SiO₂ (GNRs@Si₂₂ (B), GNRs@Si₁₅ (C), Si₂₂ and Si₁₅ indicates SiO₂ thickness in nm), and GNRs@SiO₂@GNCs plasmophores of different silica (PL₂₂ (D), PL₁₅ (E), PL= plasmophore, number indicates the thickness of silica shell in nm) upon photothermal heating using different ns laser pulses.

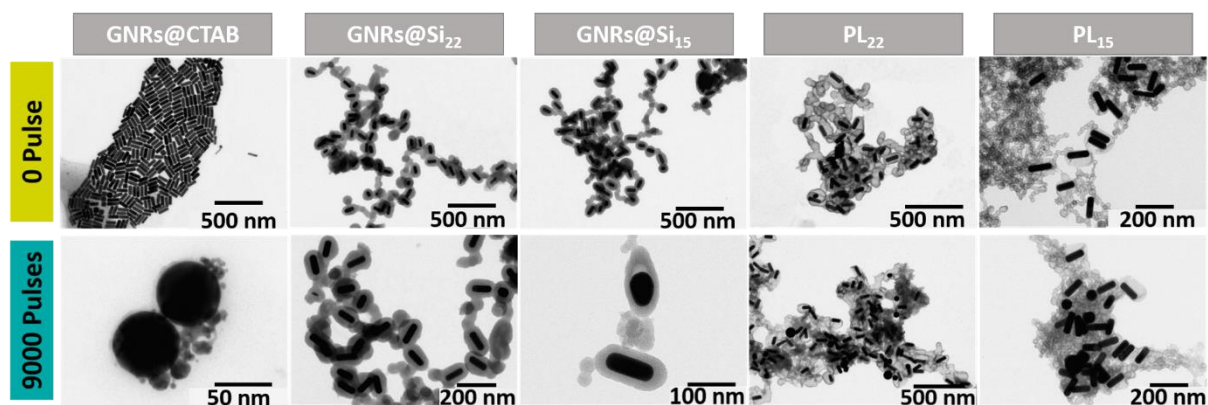


Figure S40. Photothermal-mediated reshaping of low AR GNRs@SiO₂@GNCs plasmophores. TEM images of GNRs@CTAB, GNRs@Si₂₂ and GNRs@Si₁₅, and PL₂₂ and PL₁₅ plasmophores upon photothermal heating using different ns laser pulses.

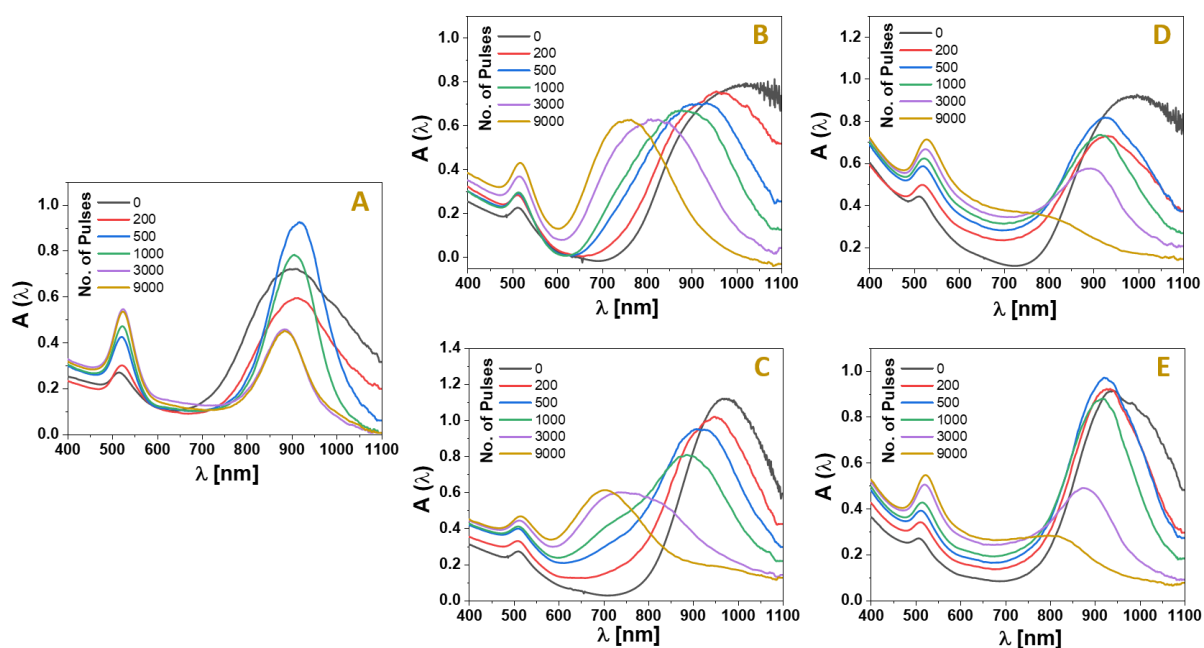


Figure S41. Photothermal-mediated reshaping of high AR GNRs@SiO₂@GNCs plasmophores. UV-vis absorption spectra of GNRs@CTAB (A), different silica thickness GNRs@SiO₂ (GNRs@Si₂₂ (B), GNRs@Si₁₅ (C), and GNRs@SiO₂@GNCs plasmophores of different silica thickness (PL₂₂ (D), PL₁₅ (E)) upon photothermal heating using different ns laser pulses.

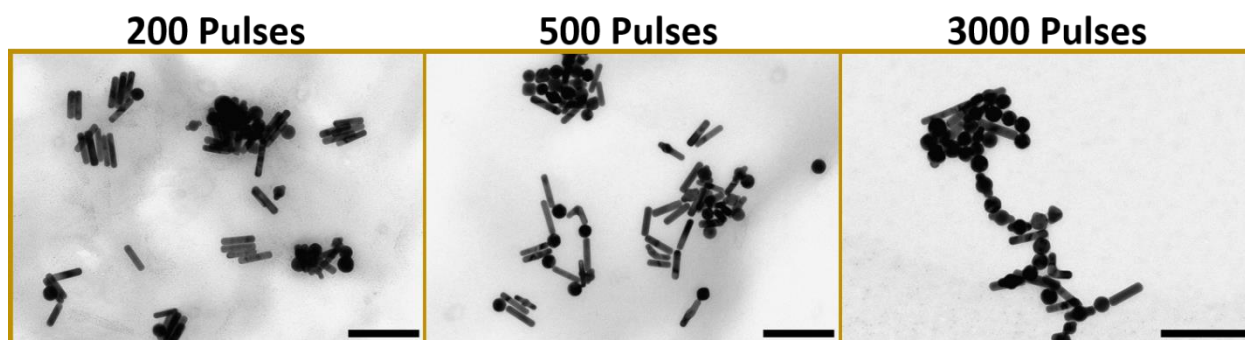


Figure S42. Photothermal-mediated reshaping of high AR GNRs. TEM images of GNRs@CTAB upon photothermal heating using different ns laser pulses. Scale bar = 200 nm.

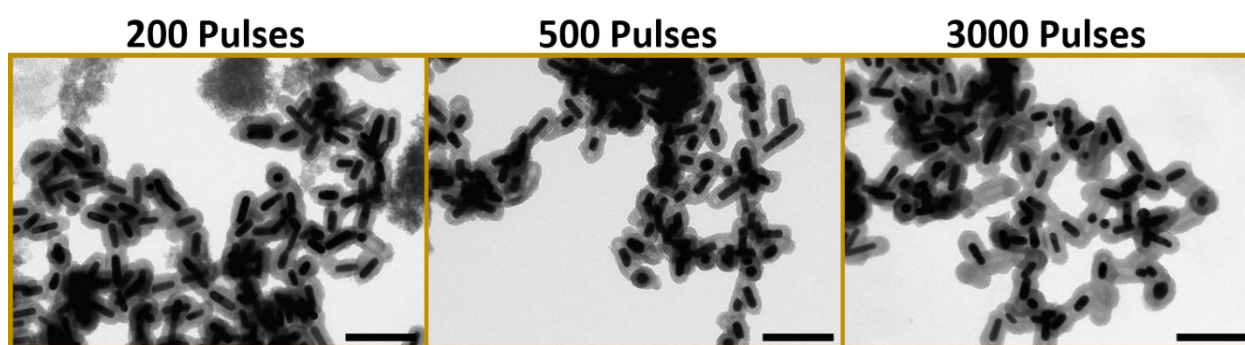


Figure S43. Photothermal-mediated reshaping of high AR GNRs@SiO₂. TEM images of GNRs@Si₂₂ upon photothermal heating using different ns laser pulses. Scale bar = 200 nm.

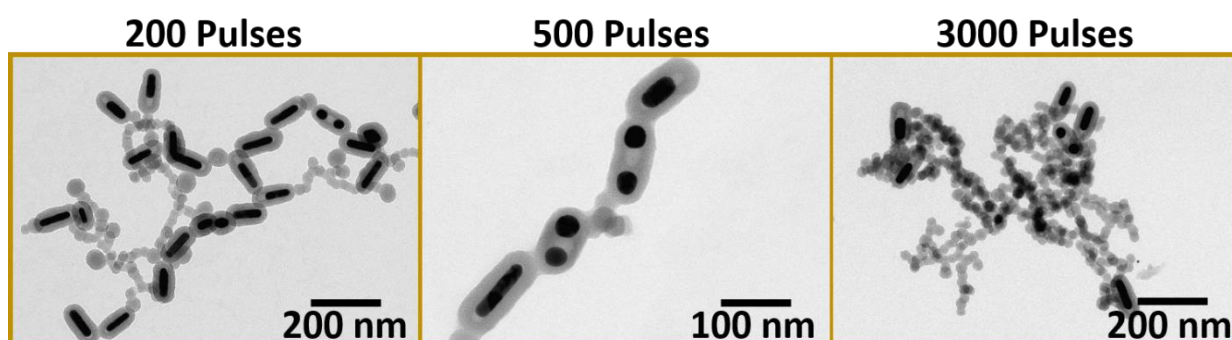


Figure S44. Photothermal-mediated reshaping of high AR GNRs@SiO₂. TEM images of GNRs@Si₁₅ upon photothermal heating using different ns laser pulses.

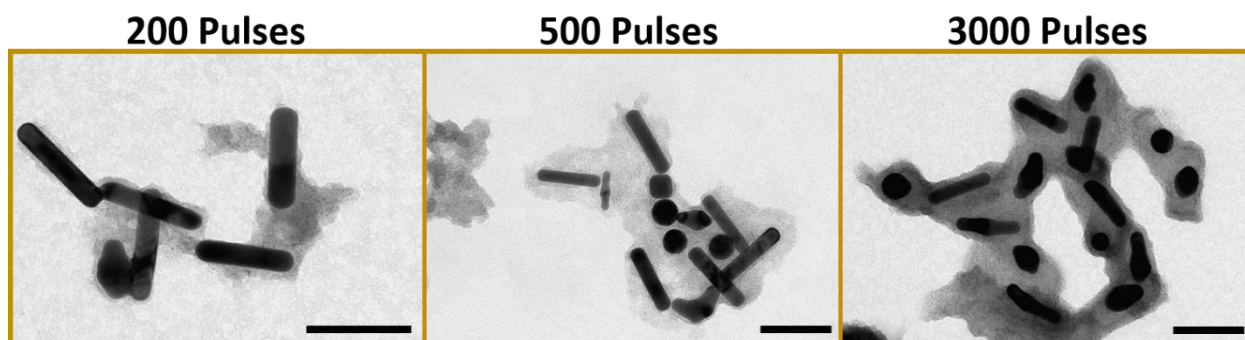


Figure S45. Photothermal-mediated reshaping of high AR GNRs@SiO₂@GNCs plasmophores. TEM images of PL₂₂ upon photothermal heating using different ns laser pulses. Scale bar = 100 nm.

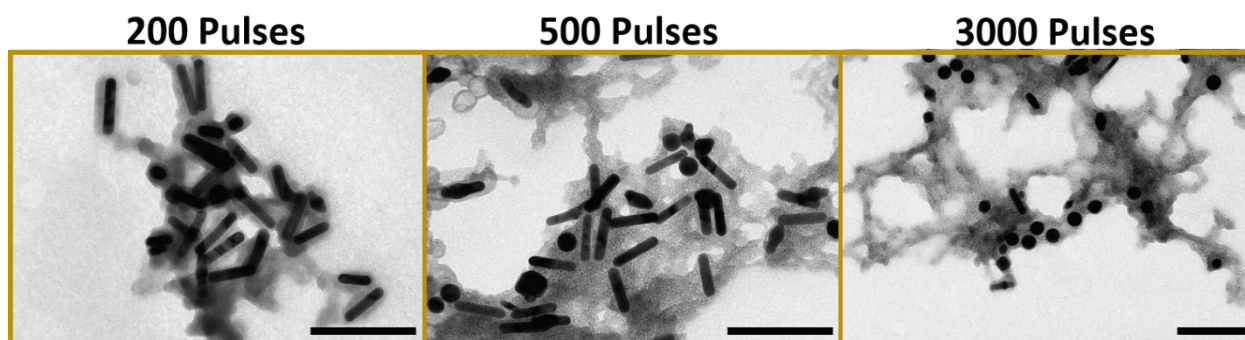
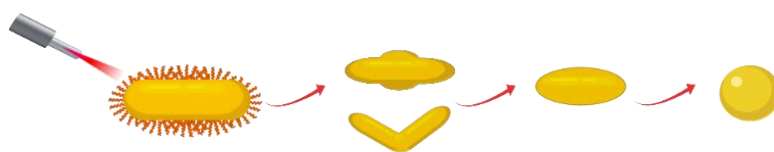
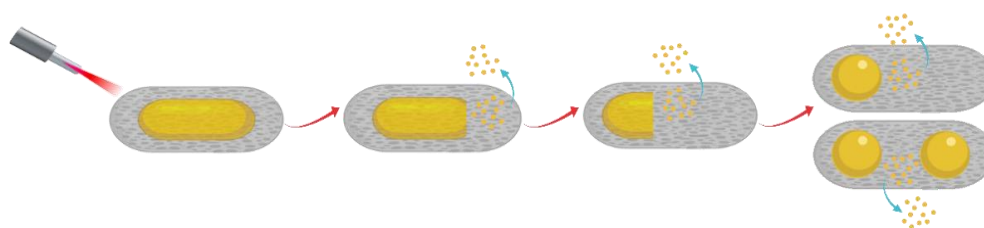


Figure S46. Photothermal-mediated reshaping of high AR GNRs@SiO₂@GNCs plasmophores. TEM images of PL₁₅ upon photothermal heating using different ns laser pulses. Scale bar = 200 nm.

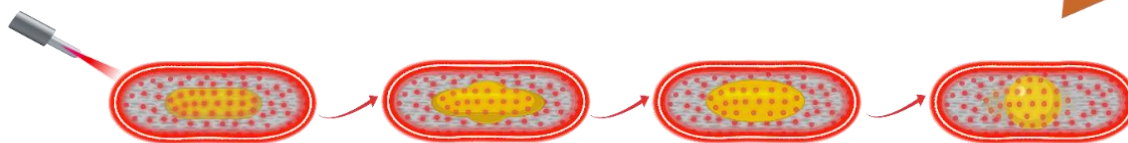
A Melting-Driven Reshaping



B Fragmentation-Driven Size Reduction



C Melting-Driven Reshaping



Scheme S1. Photothermal melting and fragmentation switching mechanism upon ns-laser irradiation of GNRs@CTAB (A), GNRs@SiO₂ (B), and GNRs@SiO₂@GNCs plasmophores (C).

14. Photoluminescence stability in O₂- and Ar-enriched environments

In order to assess the PL stability of GNCs and plasmophores their PL behavior was studied in O₂- and Ar-enriched environment. In a typical experiment, 500 μ L of GNCs or plasmophores were transferred into 5 mL transport tube. The samples were then purged with O₂ gas for 20 min and their PL spectra were recorded. The samples were subsequently purged with pure Ar gas and the PL spectra were recorded. As could be revealed from the results, O₂ gas purging

induces PL quenching of GNCs, most probably by the triplet-triplet energy transfer pathway, whereas GNRs@SiO₂@GNCs plasmophores are stable in O₂-saturated environment which means that incorporation of GNCs within a plasmophore system suppresses the O₂-induced photobleaching observed in free GNCs as well as makes plasmophores O₂-independent fluorescent system.

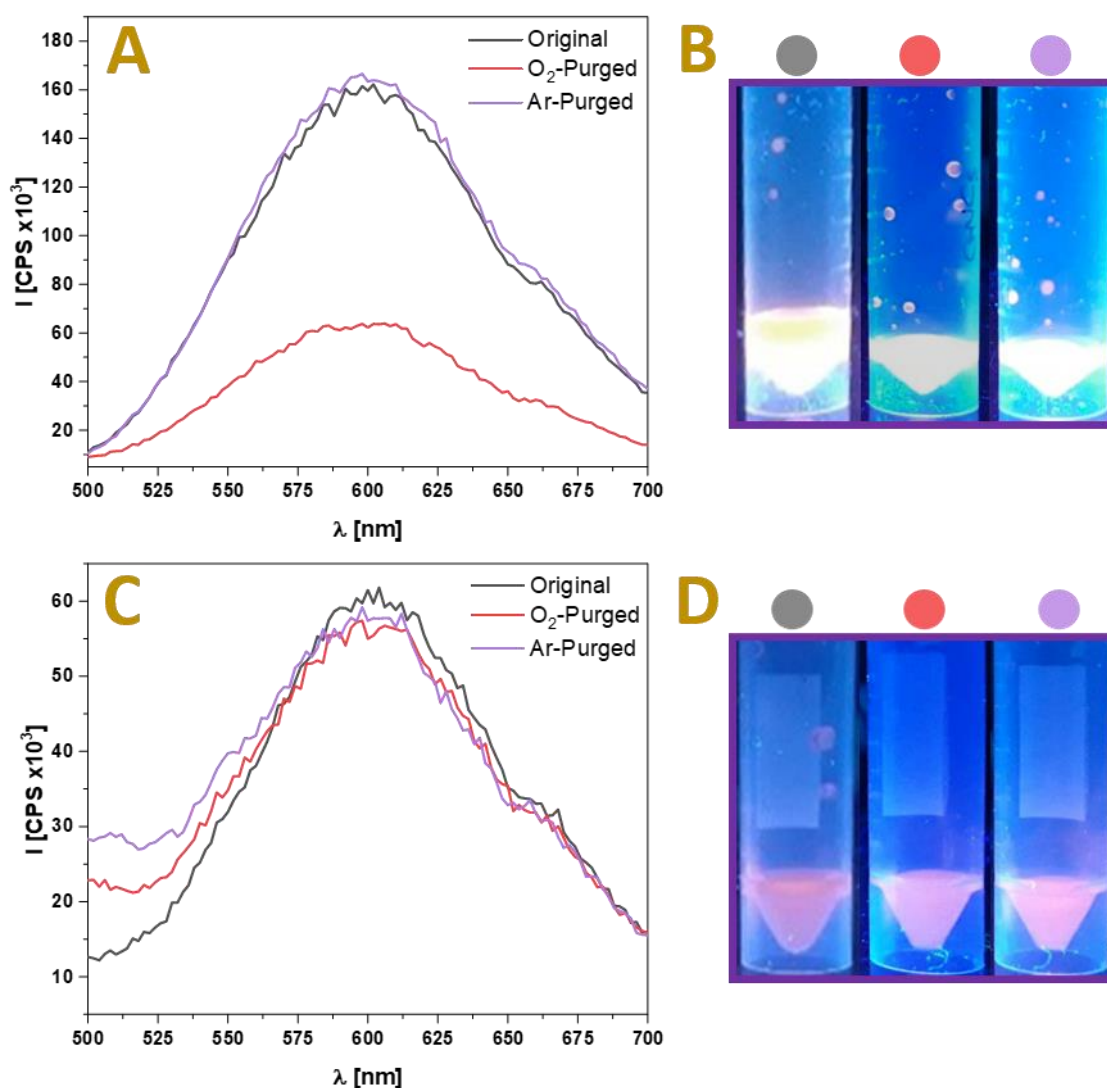


Figure S47. PL stability of GNCs and plasmophores under ambient atmosphere, O₂-, and Ar-enriched environments. (A and C) PL spectra of GNCs and plasmophores, and their corresponding photographs (B and D) under UV-lamp excitation, respectively, under ambient atmosphere, O₂-, and Ar-enriched environments.

15. Photostability of GNRs@SiO₂@GNCs plasmophores

The photostability of GNCs and plasmophores after exposure to UV light was evaluated by recording their UV-vis absorption and PL spectra. In a typical experiment, 1 mL of GNCs or plasmophores was transferred into a plastic cuvette and the samples were then irradiated by UV light using UV lamp excitation for 1 h. The UV-vis absorption and PL spectra of GNCs and plasmophores were recorded before and after UV light irradiation. The results showed no significant difference between the photostability of GNCs and GNRs@SiO₂@GNCs plasmophores.

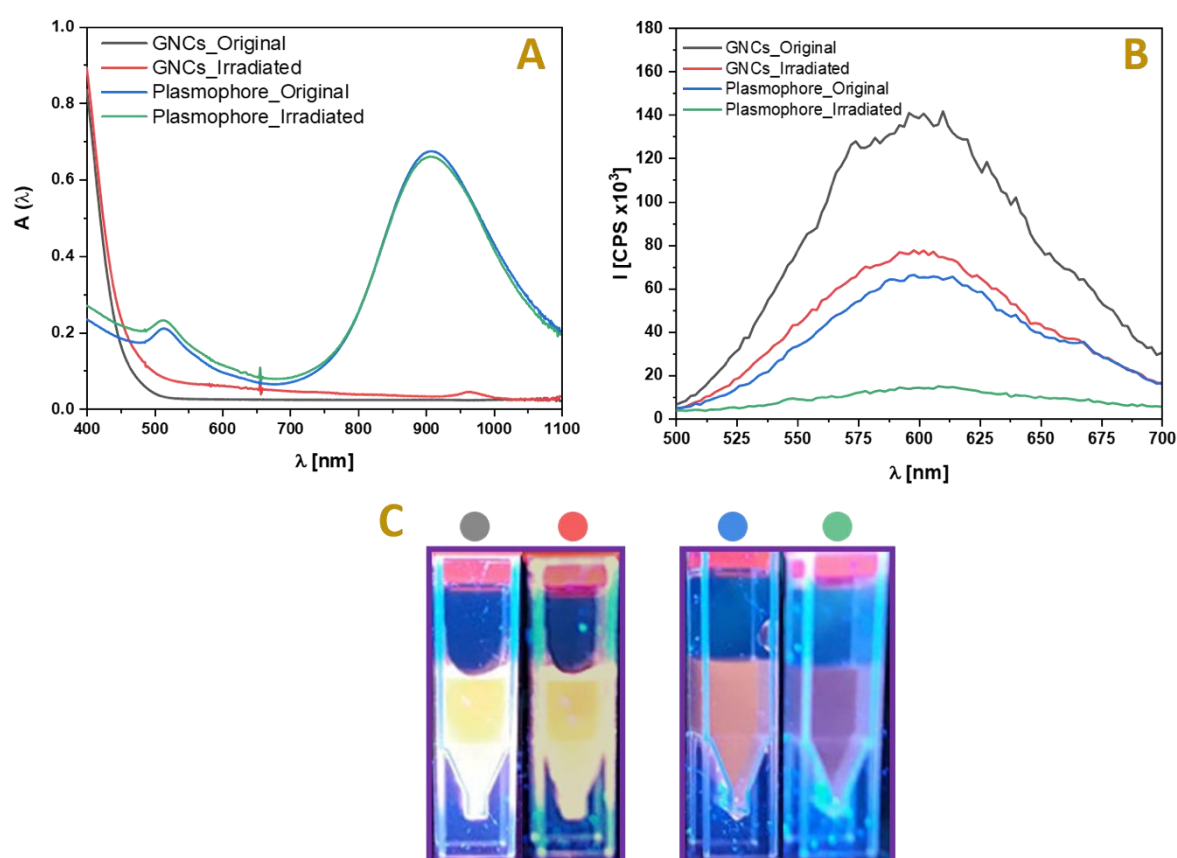


Figure S48. PL stability of GNCs and plasmophores under UV-lamp irradiation. UV-vis absorption spectra (A) and PL spectra (B) of GNCs and plasmophores before and after UV-irradiation, and their corresponding photographs (C) under UV-lamp.

16. Lumerical calculations of optical properties of GNRs@SiO₂@GNCs plasmophores

Numerical calculations of the fluorescence properties of the plasmophores were carried out using Lumerical's finite-difference time-domain software.[19] All plasmophores were modeled as cylinders with ellipsoidal end caps, characterized by the total length, the width, and the endcap radius of the GNR. For high aspect ratio rods, the length is 130 nm, the width is 26 nm, and the endcap radius is 46 nm. For low aspect ratio rods, the length is 111 nm, the width is 32 nm, and the endcap radius is 46.5 nm. The dielectric functions for gold and silica are both taken from Palik's *Handbook of Optical Constants of Solids*. [20] The background medium is water, whose dielectric function is also taken from.[20] **Figure S49 (C and D)** shows the absorption spectra for the low and high aspect ratio rods. See **Figure S18** for comparison to experimental data.

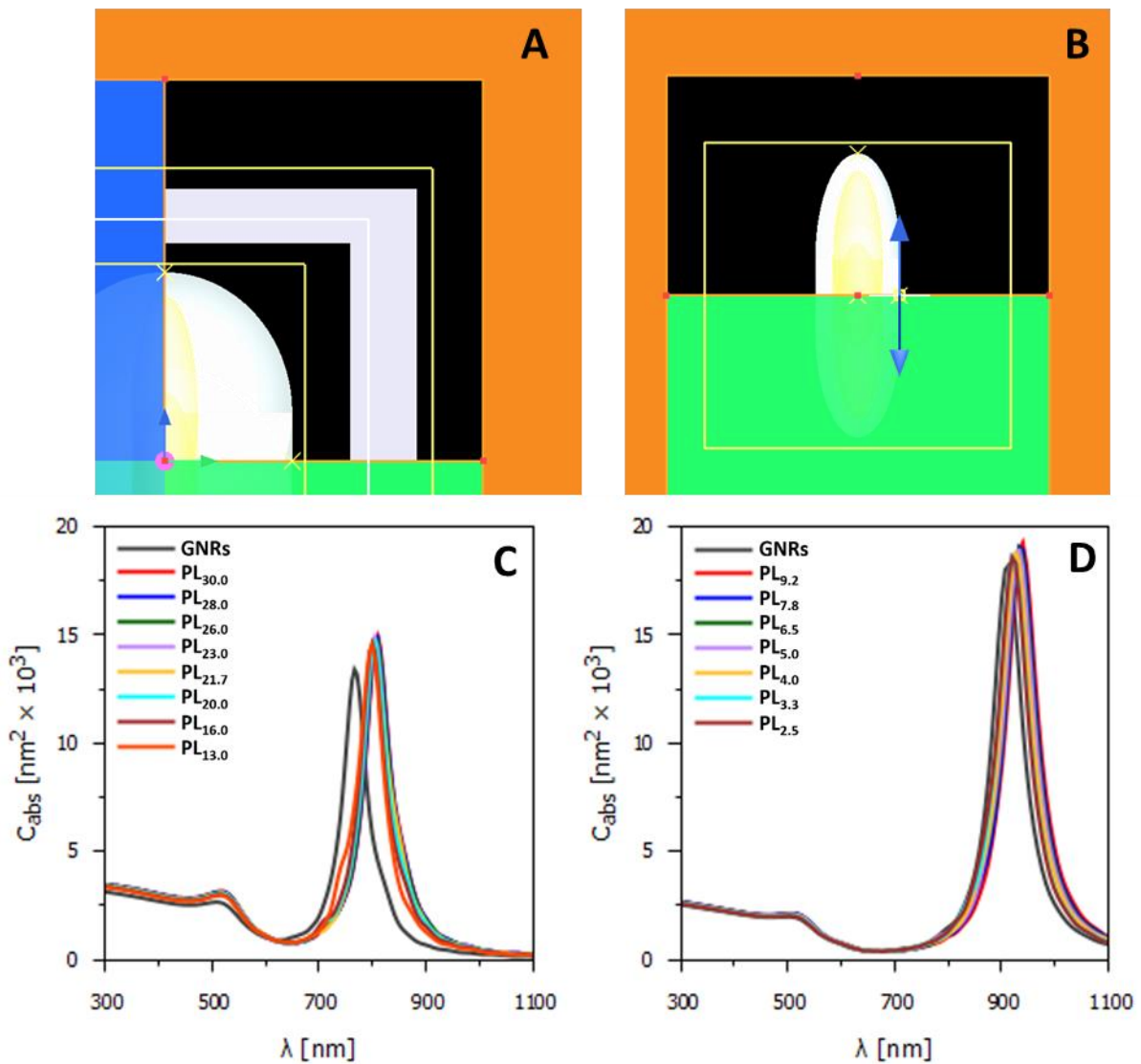


Figure S49. Schematic (not to scale) of a GNR@SiO₂ nanorod excited by a longitudinally polarized plane wave in the Lumerical FDTD simulation region [19] (A). The gray box marks the boundary of the total-field-scattered-field (TFSF) light source; inside the box, the total field (background and scattered) is calculated, while outside it, only the scattered field is calculated. The particle itself is shown in the bottom left, within the TFSF domain. Orange boundaries on the top and right are perfectly matched layers (PMLs), which absorb outgoing light without reflecting it. Where appropriate, symmetry conditions are used to reduce the size of the computational domain (shown in blue and green on the bottom and left). Yellow boxes inside and outside the TFSF domain calculate the absorption and scattering cross-sections, respectively. Yellow “X”-es mark the locations of electric field monitors. Schematic (not to scale) showing the GNR@SiO₂ nanorod excited by a dipole emitter (i.e., a fluorophore) on its surface (B). The dipole emitter is shown as a blue double-headed arrow on the right side of the particle. Orange boundaries are PMLs. Where appropriate, symmetry conditions are used to reduce the size of the computational domain (shown in green on the bottom). A quantum efficiency analysis group is used to monitor the power radiating from the dipole (small yellow box) and from the entire structure (large yellow box). This analysis group also calculates the Purcell factor, assuming the emitter has an internal efficiency of 100%. Yellow “X”-es mark the locations of electric field monitors. Absorption cross sections of (C) low AR and (D) high AR plasmophores.

Figures S50-54 show the results of theoretical calculations for the wavelength dependence of the fluorescence of low and high aspect ratio plasmophores. We model the GNCs as point-like dipole emitters on the surface of the SiO₂ shell that do not interact with each other or affect the overall absorption or scattering of the plasmophore. We present two particular points here: the tip and the equator of the plasmophore. **Figures S50** and **S52** show the fluorescence at the tip, and **Figures S51** and **S53** show the fluorescence at the equator. **Figure S54** shows the data for the tip and equator together at selected wavelengths. The low-intensity limit of the fluorescence enhancement is described by the product of the excitation rate enhancement with the quantum yield, shown in panel **A** and **B** of **Figures S50-54**, respectively.[21] The excitation rate enhancement is taken at the wavelength of the incoming light, while the quantum yield is taken at the wavelength of the emitted light. The high-intensity limit of the fluorescence enhancement is the radiative enhancement (Purcell) factor, shown in panel **C** of **Figures S50-54**. As in **Figure 2F**, the data have been multiplied by a phenomenological factor that

represents the fluorescence quenching, i.e. nonradiative losses due to quantum mechanical effects. It has form,

$$q(x) = \frac{1}{\pi} \arctan[b \times (x - x_0)] + 0.5, \quad (4)$$

Where b is a scaling factor, and x_0 is an offset. The form of $q(x)$ is chosen such that it is bounded between 0 and 1. For low aspect ratio rods (**Figures S52-54**), $b = 1 \text{ nm}^{-1}$ and $x_0 = 22 \text{ nm}$. For high aspect ratio rods (**Figures 2, S50-51**), $b = 3 \text{ nm}^{-1}$ and $x_0 = 6.2 \text{ nm}$. In the limit that the shells are very (infinitely) thick, the GNCs are completely decoupled from the GNR, and the Purcell factor approaches a constant value.

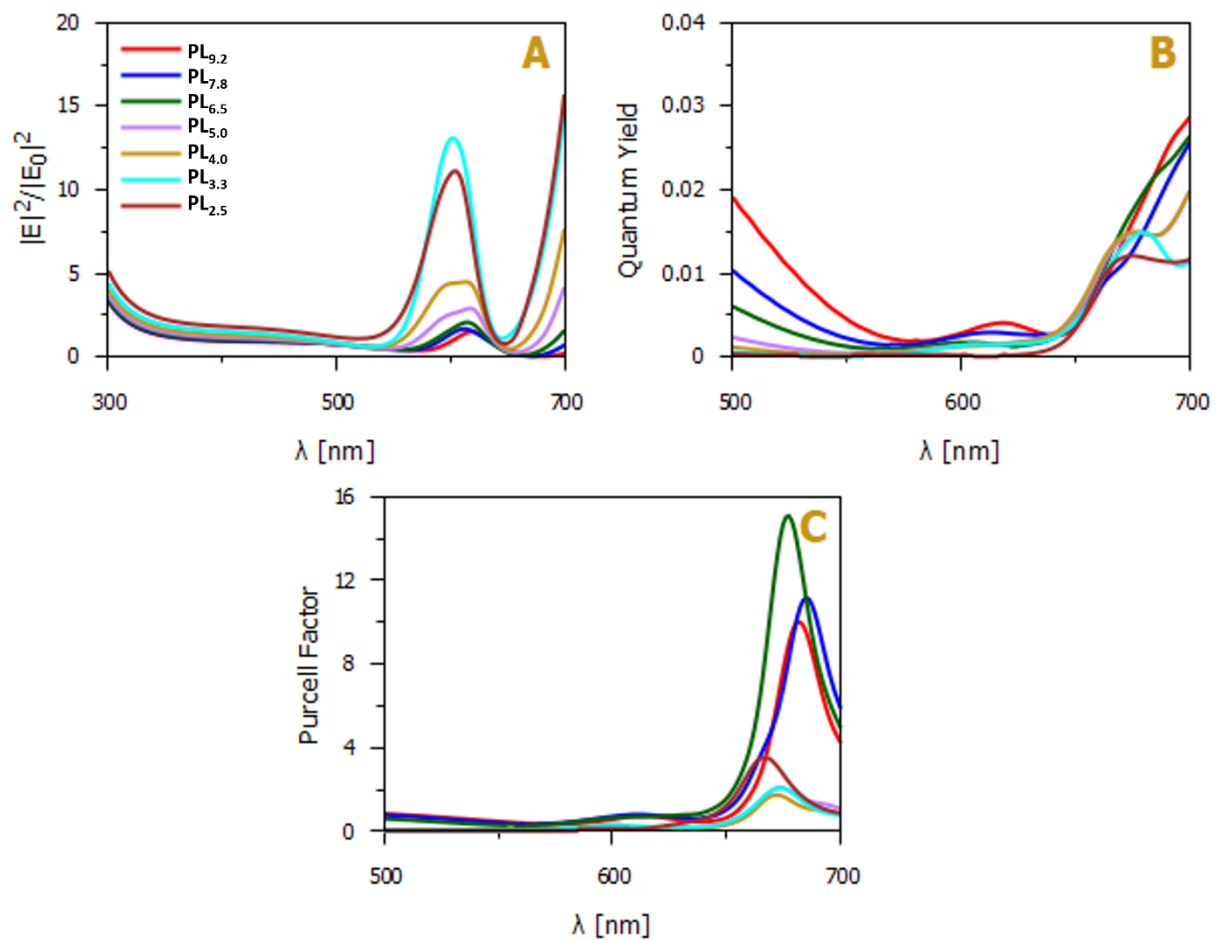


Figure S50. Fluorescence enhancement at the tip of high aspect ratio plasmophores. (A) Electric field enhancement squared, (B) quantum yield, and (C) Purcell factor.

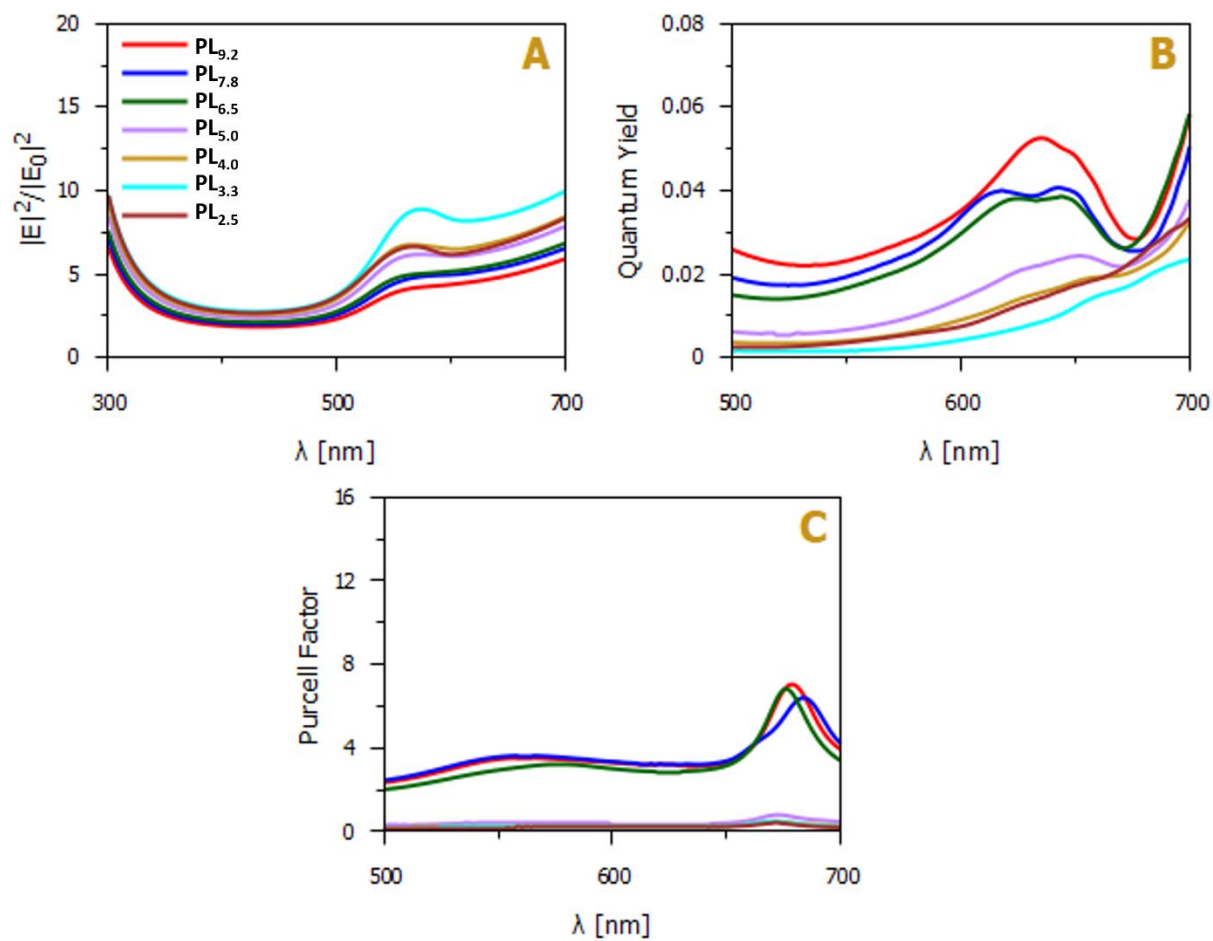


Figure S51. Fluorescence enhancement at the equator of high aspect ratio plasmophores. (A) Electric field enhancement squared, (B) quantum yield, and (C) Purcell factor.

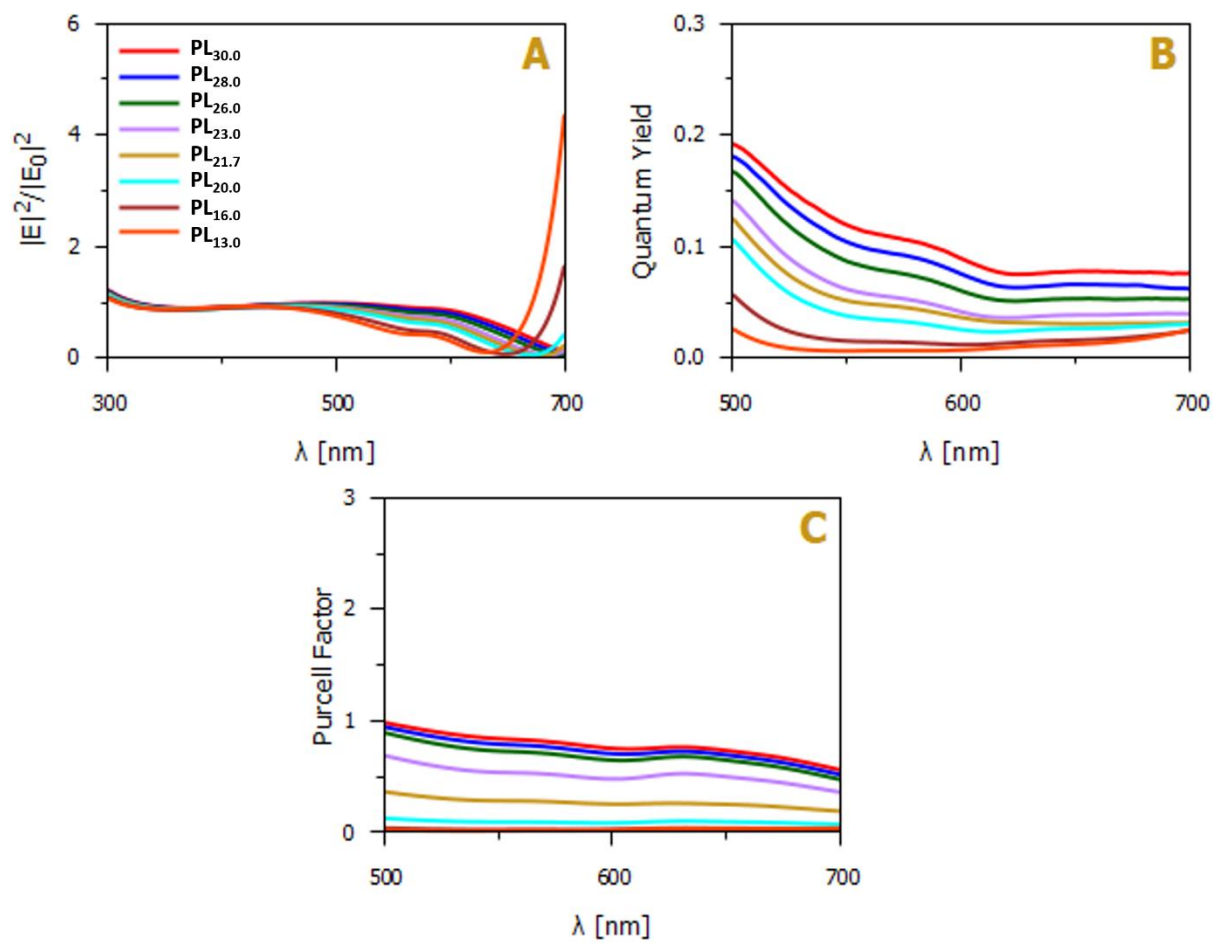


Figure S52. Fluorescence enhancement at the tip of low aspect ratio plasmaphores. (A) Electric field enhancement, (B) quantum yield, and (C) Purcell factor.

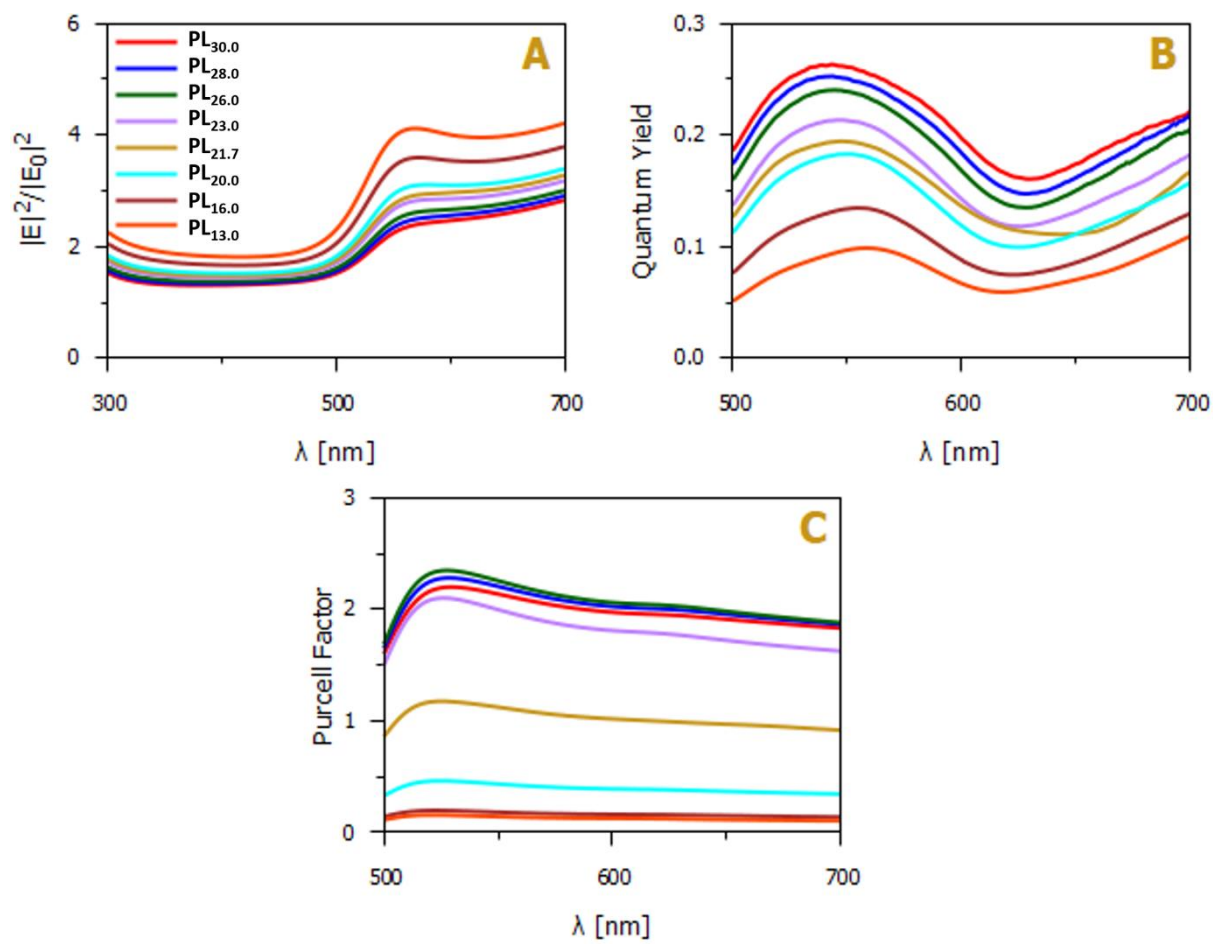


Figure S53. Fluorescence enhancement at the equator of low aspect ratio plasmaphores. (A) Electric field enhancement squared, (B) quantum yield, and (C) Purcell factor.

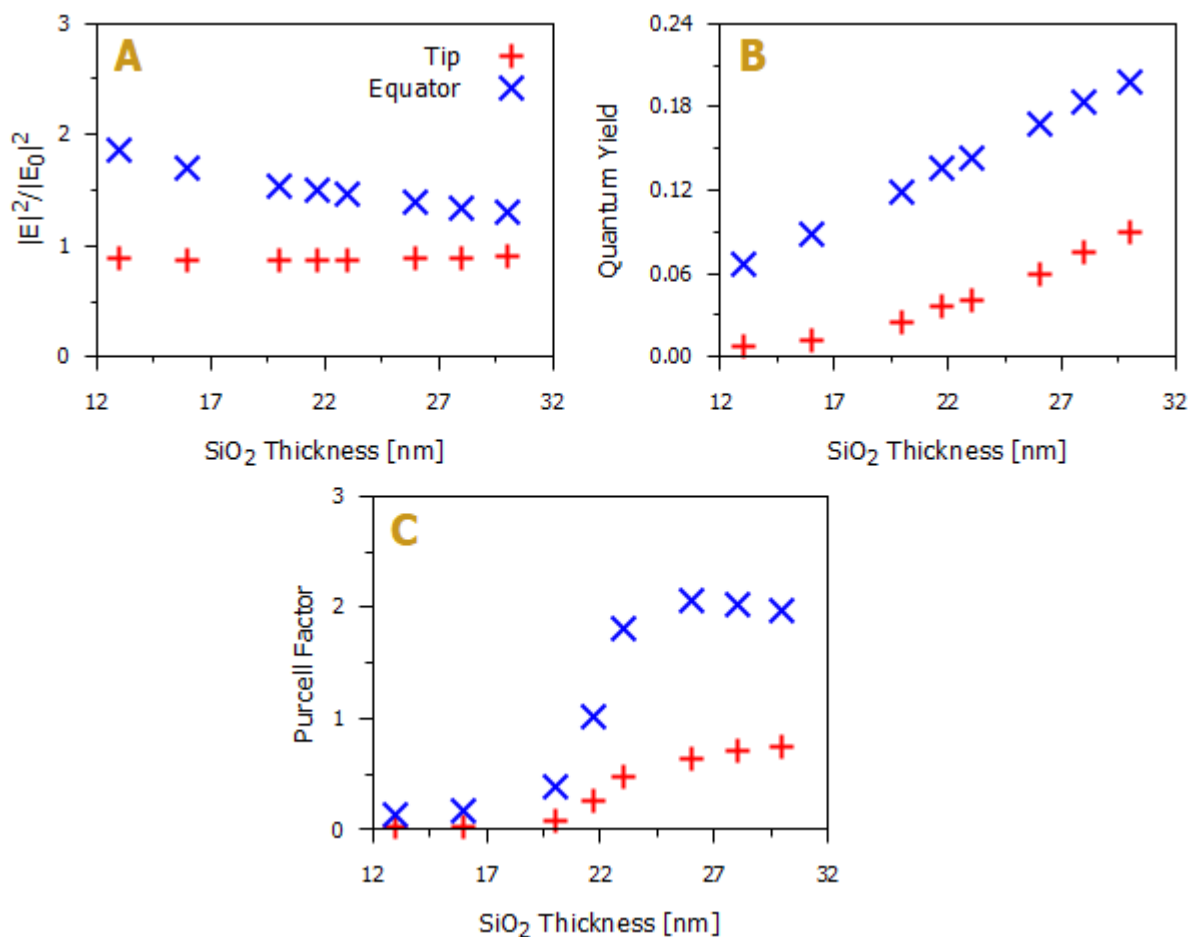


Figure S54. Shell thickness versus fluorescence for low AR plasmophores. (A) Electric field enhancement squared at 365 nm at the surface of the GNR@SiO₂. (B) Quantum yield of a dipole emitter at 600 nm at the surface of the GNR@SiO₂ antenna. (C) Purcell factor at 600 nm at the surface of the GNR@SiO₂ complex.

17. Photothermal simulations of GNRs@SiO₂@GNCs plasmophores

In order to gain further insight into the photothermal stability displayed by the plasmophores (see **Figures S39-46**), we performed finite element method (FEM) simulations with the commercial software COMSOL Multiphysics. The geometry of the nanorod and material properties used in the simulations were the same as those described in the previous section. Notice that this means we assumed, for simplicity, that the dielectric functions were temperature-independent. The GNCs were modeled as portions of spheres with a radius of 1 nm spread across the outer SiO₂ surface, as shown in **Figure 6A**, for an SiO₂ thickness of 2.5 nm. The photothermal simulation proceeded in two steps: (i) an optical simulation was performed to determine the ohmic heat dissipation at every point in the plasmophore, and (ii) a time-dependent thermal simulation was carried out with a heat source determined by the

previous step. The strength of the incident electric field used in the first step was determined by the pump fluence of 320 mJ/cm^2 and a wavelength of 1064 nm was used.

18. References

1. Nagashima, S., et al. *A high-accuracy rotation estimation algorithm based on 1D phase-only correlation*. in *International Conference Image Analysis and Recognition*. 2007. Springer.
2. Foroosh, H., J.B. Zerubia, and M. Berthod, *Extension of phase correlation to subpixel registration*. *IEEE transactions on image processing*, 2002. **11**(3): p. 188-200.
3. Takita, K., et al., *High-accuracy subpixel image registration based on phase-only correlation*. *IEICE transactions on fundamentals of electronics, communications and computer sciences*, 2003. **86**(8): p. 1925-1934.
4. Yan, H. and J.G. Liu. *Robust Phase Correlation based Motion Estimation and Its Applications*. in *BMVC*. 2008.
5. Ye, X., et al., *Using Binary Surfactant Mixtures To Simultaneously Improve the Dimensional Tunability and Monodispersity in the Seeded Growth of Gold Nanorods*. *Nano Letters*, 2013. **13**(2): p. 765-771.
6. Orendorff, C.J. and C.J. Murphy, *Quantitation of Metal Content in the Silver-Assisted Growth of Gold Nanorods*. *J. Phys. Chem. B*, 2006. **110**(9): p. 3990-3994.
7. Luo, Z., et al., *From Aggregation-Induced Emission of Au(I)-Thiolate Complexes to Ultrabright Au(0)@Au(I)-Thiolate Core-Shell Nanoclusters*. *Journal of the American Chemical Society*, 2012. **134**(40): p. 16662-16670.
8. Gole, A. and C.J. Murphy, *Polyelectrolyte-Coated Gold Nanorods: Synthesis, Characterization and Immobilization*. *Chemistry of materials*, 2005. **17**(6): p. 1325-1330.
9. Stöber, W., A. Fink, and E. Bohn, *Controlled growth of monodisperse silica spheres in the micron size range*. *Journal of Colloid and Interface Science*, 1968. **26**(1): p. 62.
10. Abadeer, N.S., et al., *Distance and plasmon wavelength dependent fluorescence of molecules bound to silica-coated gold nanorods*. *ACS nano*, 2014. **8**(8): p. 8392-8406.
11. Cifuentes, A., J.L. Bernal, and J.C. Diez-Masa, *Determination of critical micelle concentration values using capillary electrophoresis instrumentation*. *Analytical Chemistry*, 1997. **69**(20): p. 4271-4274.
12. Gorelikov, I. and N. Matsuura, *Single-Step Coating of Mesoporous Silica on Cetyltrimethyl Ammonium Bromide-Capped Nanoparticles*. *Nano Letters*, 2008. **8**(1): p. 369-373.
13. Nooney, R.I., et al., *Self-assembly of mesoporous nanoscale silica/gold composites*. *Langmuir*, 2003. **19**(18): p. 7628-7637.
14. Xie, J., Y. Zheng, and J.Y. Ying, *Protein-directed synthesis of highly fluorescent gold nanoclusters*. *Journal of the American Chemical Society*, 2009. **131**(3): p. 888-889.
15. van der Linden, M., et al., *Insights into the Synthesis Mechanism of Ag29 Nanoclusters*. *The Journal of Physical Chemistry C*, 2018. **122**(49): p. 28351-28361.
16. Wandelt, B., et al., *Fluorescent molecularly imprinted polymer studied by time-resolved fluorescence spectroscopy*. *Polymer*, 2002. **43**(9): p. 2777-2785.
17. Jones, M. and G.D. Scholes, *On the use of time-resolved photoluminescence as a probe of nanocrystal photoexcitation dynamics*. *Journal of Materials Chemistry*, 2010. **20**(18): p. 3533-3538.
18. Fery-Forgues, S. and D. Lavabre, *Are fluorescence quantum yields so tricky to measure? A demonstration using familiar stationary products*. *Journal of chemical education*, 1999. **76**(9): p. 1260.
19. Lumerical Solutions, I.; Available from: <http://www.lumerical.com/tcad-products/fdtd/>.
20. Palik, E.D., *Handbook of optical constants of solids*. Vol. 3. 1998: Academic press.
21. Novotny, L. and B. Hecht, *Principles of nano-optics*. 2012: Cambridge university press.